Materials Chemistry and Physics 271 (2021) 124936

Contents lists available at ScienceDirect

Materials Chemistry and Physics

journal homepage: www.elsevier.com/locate/matchemphys

Study of microstructure and mechanical behaviour of aluminium alloy hybrid composite with boron carbide and graphene nanoplatelets

Mahmood Khan [a,d,*], Rafi Ud Din [b], Muhammad Abdul Basit [a], Abdul Wadood [a], Syed Wilayat Husain [a], Shahid Akhtar [c], Ragnhild Elizabeth Aune [d]

[a] Department of Materials Science and Engineering, Institute of Space Technology, Islamabad, 44000, Pakistan
[b] Materials Division, Pakistan Institute of Nuclear Science and Technology, Nilore, 45650, Pakistan
[c] Norsk Hydro, Karmøy Primary Production, Hydrovegen, N-4265, Håvik, Norway
[d] Department of Materials Science and Engineering, Faculty of Natural Sciences, Norwegian University of Science and Technology, 7491, Trondheim, Norway

HIGHLIGHTS

- A novel hybrid aluminium alloy (6061) composite containing boron carbide and graphene nanoplatelets is presented.
- Electron Back Scattered Diffraction is employed to investigate the hybrid composite's microstructure.
- Improvements in mechanical properties of the hybrid composite are recorded in fabricated and thermally aged matrices.
- Detailed fractography of the novel hybrid composite is carried to investigate the strengthening and deformation mechanism.

GRAPHICAL ABSTRACT

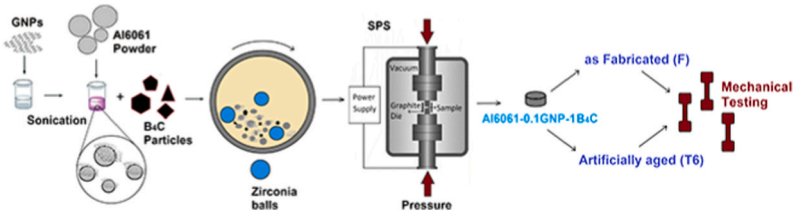

ARTICLE INFO

Keywords:
Aluminium matrix composite
Graphene nanoplatelets (GNPs)
Spark plasma sintering (SPS)
Boron carbide (B_4C)
Hybrid composite

ABSTRACT

Lightweight materials with superior designs and improved properties have always been in demand of the aerospace and automobile industries for improved performance. Spark plasma sintering was employed in the present study for the fabrication of a hybrid composite of boron carbide and graphene nanoplatelets. Reference samples and composites with 0.1 wt% GNPs, 1 wt% B_4C and hybrid combination containing 0.1 wt% GNPs and 1 wt% B_4C in Al6061 matrix were prepared. All the samples were divided into two groups, namely; as fabricated and artificially age hardened (T6). Electron backscattered diffraction technique was employed to evaluate the microstructure along with the optical and scanning electron microscopy. Various illustrative models have been conceived to describe the physical behaviours of the composites. Improvements in hardness (33% & 50%) and tensile strength (11% & 20%) were exhibited by the hybrid composite in F and T6 conditions, respectively. The strengthening mechanism is explained with the help of fractography. The fractured surfaces revealed uniform distribution of reinforcements and extensive crack deflection.

* Corresponding author. Department of Materials Science and Engineering, Faculty of Natural Sciences, Norwegian University of Science and Technology, 7491, Trondheim, Norway.
E-mail addresses: mahmood.khan@ntnu.no, mahmoodkhan77@gmail.com (M. Khan), rafi368@yahoo.com (R.U. Din), absaim@gmail.com (M.A. Basit), abdul.wadood@ist.edu.pk (A. Wadood), wilayat.hussain@ist.edu.pk (S.W. Husain), shahid.akhtar@hydro.com (S. Akhtar), ragnhild.aune@ntnu.no (R.E. Aune).

https://doi.org/10.1016/j.matchemphys.2021.124936
Received 11 September 2020; Received in revised form 22 May 2021; Accepted 4 July 2021
Available online 6 July 2021

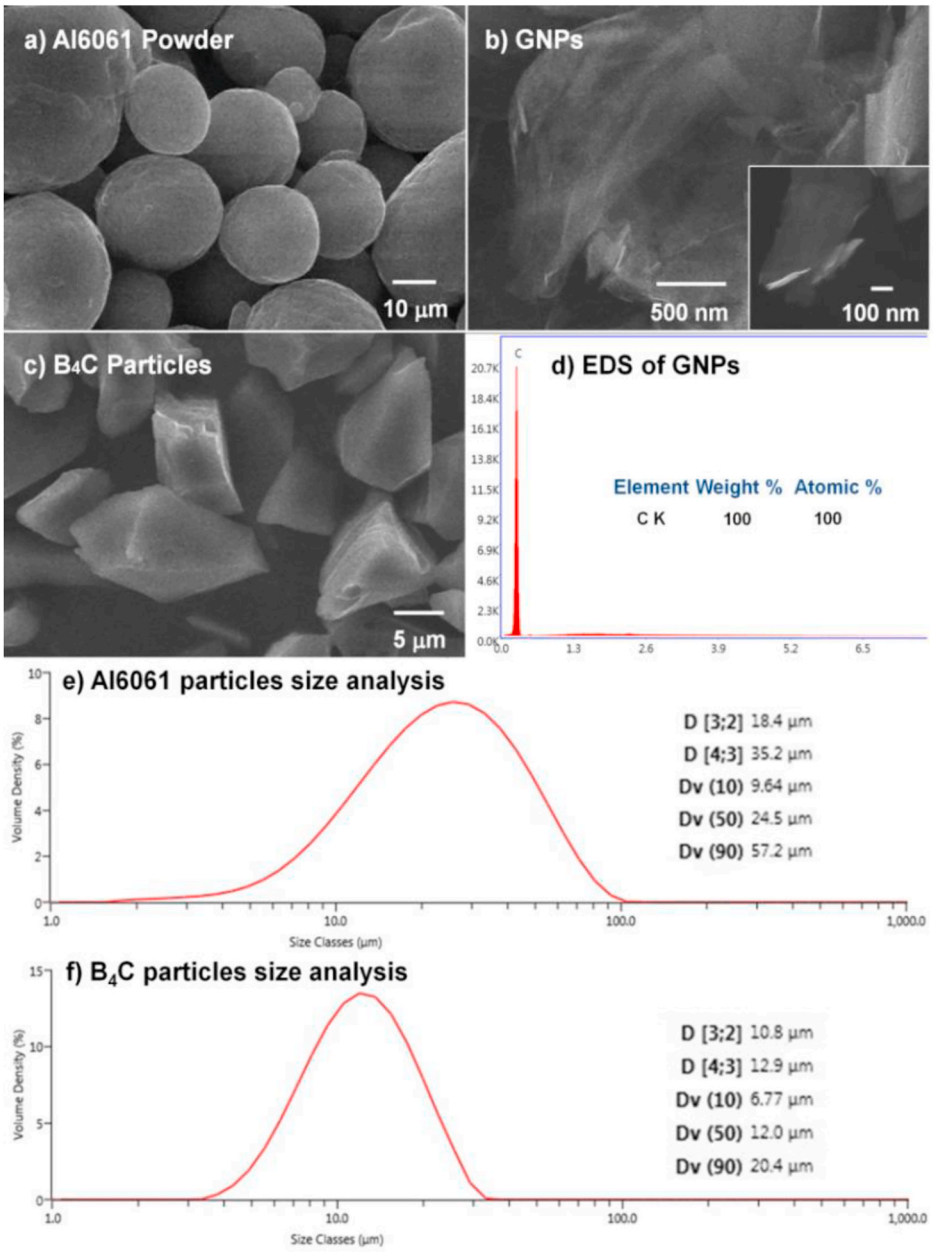

Fig. 1. SEM images of raw materials showing: (a) Al6061 particles, (b) GNPs, (c) B_4C particles, (d) EDS of GNPs, (e) particle size analysis of Al6061 and (f) particle size analysis of B_4C particles.

1. Introduction

The development of lightweight and high strength materials has always been a demand of industries to meet performance and economic benefits. Aluminium and its alloys have proved to be an inevitable choice due to their comparatively lower density, moderate strength, ease of formability and response to heat treatment processes. Aluminium matrix composites (AMCs) exhibited improved mechanical properties when compared to aluminium and/or its alloy [1]. Generally, ceramic reinforcements like alumina (Al_2O_3), silica (SiC), Boron Carbide (B_4C), titanium carbide (TiC), aluminium nitride (AlN) and many more have been added to aluminium and its alloys [2]. Carbonaceous reinforcements in the form of fibres [3] and nano reinforcements [4] have also been successful additions in aluminium and its alloys.

B_4C is among the strongest ceramics available with a variety of applications like bulletproof vests, blasting/cutting nozzles, neutron absorber, brake liners, anti-ballistic armour plating, and many others [5]. It has been used as reinforcement in aluminium and alloys to result in increased hardness [6]. Composites of B_4C in aluminium and its alloys have been developed to tailor the physical and mechanical properties [7]. Recent advances in carbonaceous nanomaterials emphasise the importance of exploring the properties of carbon nanotubes (CNTs) and Graphene Nanoplatelets (GNPs) in AMCs for engineering applications. The incorporation of CNTs [8] and GNPs [9] in AMCs have been studied. The physical and mechanical properties of graphene are highly suitable to make it a potential nano reinforcement in AMCs. The properties such as thermal conductivity (5000W/m.K), high modulus of elasticity (1 TPa) [10] and large surface area (~2630 m^2/g) provides an opportunity to explore AMCs with controlled interfacial properties [11]. The addition of GNPs up to a certain limit has substantiated improvements in the overall mechanical properties of the AMCs [12].

The selection of processing method determines the distribution of reinforcement and properties of the final composite. All of the conventional metal processing methods with variants have been employed for

the development of AMCs. Stir casting [13], pressure infiltration [14], squeeze casting [15], friction stir processing [16], Spark Plasma Sintering (SPS) [17], powder metallurgy (PM) accompanied by pressure less [18] and pressure-assisted [19] sintering, etc. have been reported for the successful processing of AMCs. Secondary processing is optionally employed to obtain near theoretical densities and texture control of the final AMC's properties. For this purpose, hot pressing [20], extrusion [21], roll bonding [22], rolling [23], and forging [24] have been employed as the secondary processing techniques. A dual-processing approach is additionally employed for the final shaping of the composites and to ensure minimum porosity, texture modification for enhancement in mechanical properties. However, the addition of a secondary processing technique, adds cost to the processing of AMCs. Thus a need for a minimum processing cost with a minimum exposure of the AMCs to high temperatures is encouraged to avoid interfacial reactions and the segregation of reinforcements.

Among all the other primary processing techniques, SPS has attracted substantial attention over the past few years for the processing of ceramics and ceramic matrix composites [25]. For AMCs, SPS is lesser explored compared to stir casting, PM, squeeze casting, etc. In SPS, the plasma generated due to current arching has an effect of cleansing the impurities from the metallic particle surface. This feature of SPS enhances the heat transfer which is essential to produce a stronger bond between the matrix and the reinforcement particles [26]. The confined generation of heat at the contact points of the powder particles also results in the breakage of the characteristic oxide layer on the aluminium powders [27]. The exposed metal surface sinters into denser, stronger grains compared to conventional PM sintering [28]. Due to these distinct features, SPS has become a favourable choice for researchers to explore the spark plasma sintered (SPSed) AMCs.

Particles-reinforced AMCs are attracting vast potential in the aerospace and automotive industries due to their improved mechanical properties and economic viabilities. Al-GNPs composites are mostly based on pure aluminium matrix [29]. Aluminium alloys have also been reported to respond to incremental strength, e.g. Al–Mg & Cu alloy [30], Al2124 [31], Al4043 [32], 5xxx series [7], etc. 6xxx series has been explored recently by some researchers [33]. Thus emphasising the fact of increasing research and applications based potential of Al6061-GNPs composites. Al6061 has been reinforced by many ceramics [34,35] as well as carbonaceous reinforcements; carbon fibres [36], CNTs [37] and GNPs [38]. B_4C as reinforcement in AMCs is still among the attractive and potential candidates. Optimised contents of GNPs and B_4C in the aluminium matrix as individual reinforcements have been reported to result in microstructure evolution and tailored mechanical properties. Hybrid AMCs have also proved to exhibit incremental strength compared to the addition of single reinforcement in the same matrices [39,40]. An effort is hereby carried out to develop an understanding of hybrid composite processed through SPS and explore the effect of multiscale reinforcements containing GNPs and micron-sized B_4C at minimum wt.% addition in Al6061 matrix. Furthermore, a comparative study is carried out in (as) fabricated (F) and thermally aged (T6) conditions to establish the contribution of reinforcements as individual and in hybrid combination.

One of the aims of this study is to develop AMCs with GNPs and B_4C as individual and in a hybrid combination of reinforcements, processed by SPS. Al6061 matrix was chosen due to its heat treatability and wide structural applications. Lower wt.% of GNPs and B_4C were selected with an approach to establish the contribution of binary reinforcements based on previous studies of the authors. The effect of dual reinforcements in fabricated (F) and thermally aged (T6) matrices, is explored and a comparative approach is adopted for explanation in the light of relevant studies. Another aim of the present study is to employ a combination of solution treatment and ball milling to process the composite powders, followed by cold compaction and SPS for consolidation and sintering, respectively. Composite powders were characterized by energy dispersive spectroscopy (EDS), scanning electron microscopy (SEM), Fourier transform infrared spectroscopy (FTIR) and Raman spectroscopy. SPSed reference and composites were characterized by optical microscopy (OM), SEM, Electron Backscatter Diffraction (EBSD), x-ray diffraction (XRD), microhardness and tensile tests.

Table 1
Details of Al6061 showing: a) nominal composition in wt.% as measured from ICPMS, b) SPS parameters and c) description of SPS reference and composites.

a) Nominal composition of Al6061 powder

	Mg	Si	Cu	Cr	Fe	Zn	Al
Al6061	1.02	0.54	0.29	0.09	0.05	0.004	Balance

b) SPS parameters

Temperature	Pressure	Heating Rate	Holding time	Vacuum
450 °C	60 MPa	50 °C/min	10 min	10 Pa

c) Composites description used in the manuscript

Sr. No.	Sample	Description	Thermal Condition	
1.	Al6061	Reference sample	F	T6
2.	Al6061-0.1GNP	0.1 wt% GNPs	F	T6
3.	Al6061–1B_4C	1 wt% B_4C	F	T6
4.	Al6061-0.1GNP-1B_4C	0.1 wt% GNPs + 1 wt% B_4C	F	T6

2. Experimentation

2.1. Materials

Al6061 powder (Product Code ALM-6061-P) in spherical 'morphology (Fig. 1a) with composition as shown in Table 1a and nominal size of ~25 μm (Fig. 1e) was used as matrix material. Al6061 powder composition was measured by Inductively Coupled Plasma Mass Spectroscopy (ICPMS) and the particles size was measured by Mastersizer 3000, Malvern Instruments, UK. SEM images of raw materials; Al6061 powders, B_4C particles (Article No. K520-2) and Raw GNPs (Article No. C952) are shown in Fig. 1. B_4C with particle size ~10 μm (Fig. 1f) and GNPs with an approximate length of 1–5 μm and average thickness of 4–12 nm were purchased from Hongwu International Group, China. Fig. 1c shows B_4C particles, Fig. 1b and d shows SEM and EDS of GNPs in raw, as received form.

2.2. Composite fabrication

Table 1c summarizes the reference and composites prepared by SPS for this study. GNPs in calculated quantity for Al6061-0.1GNP and Al6061-0.1GNP-1B_4C composites were weighed and dispersed in 70/30% water-ethanol solution [41]. The mixtures were sonicated in UP400S probe sonicator (Hielscher, Germany) for 1 h at a frequency of 24 kHz. The respective weighed quantity of Al6061 matrix powder was added to the solution followed by sonication for 15 min [42]. A similar mixing approach has been published by the authors elsewhere [43]. The SEM images of GNPs on a silicon wafer after sonication are shown in the inset of Fig. 1b. Planetary ball mill PM 100 (RETSCH, Germany) was used for milling with Zirconia cylindrical balls, as grinding media. The ratio of the grinding media mass to the milling composite mass was 10:1. The ball milling parameters are selected from the published practice by Rafi et al. [44]. Stearic acid, as a process control agent in 0.02 wt% of the charge mass was used. Ball milling was carried out at 200 rpm for 1hr in Argon atmosphere to avoid exposure of the powder surfaces to oxidation. An interval of 5 min was given after 30 min to avoid overheating of the charge mass during ball milling.

The ball-milled reference and composite powders were pre-compacted in a graphite die with Torin® Big RedTM 10 Hydraulic Press (Model TY10003) at 200 MPa. The secondary compaction was accompanied by sintering in SPS – 825 Dr. Sinter (Fuji Electronic Industrial Co. Ltd. Japan). Table 1b shows the selected SPS parameters to

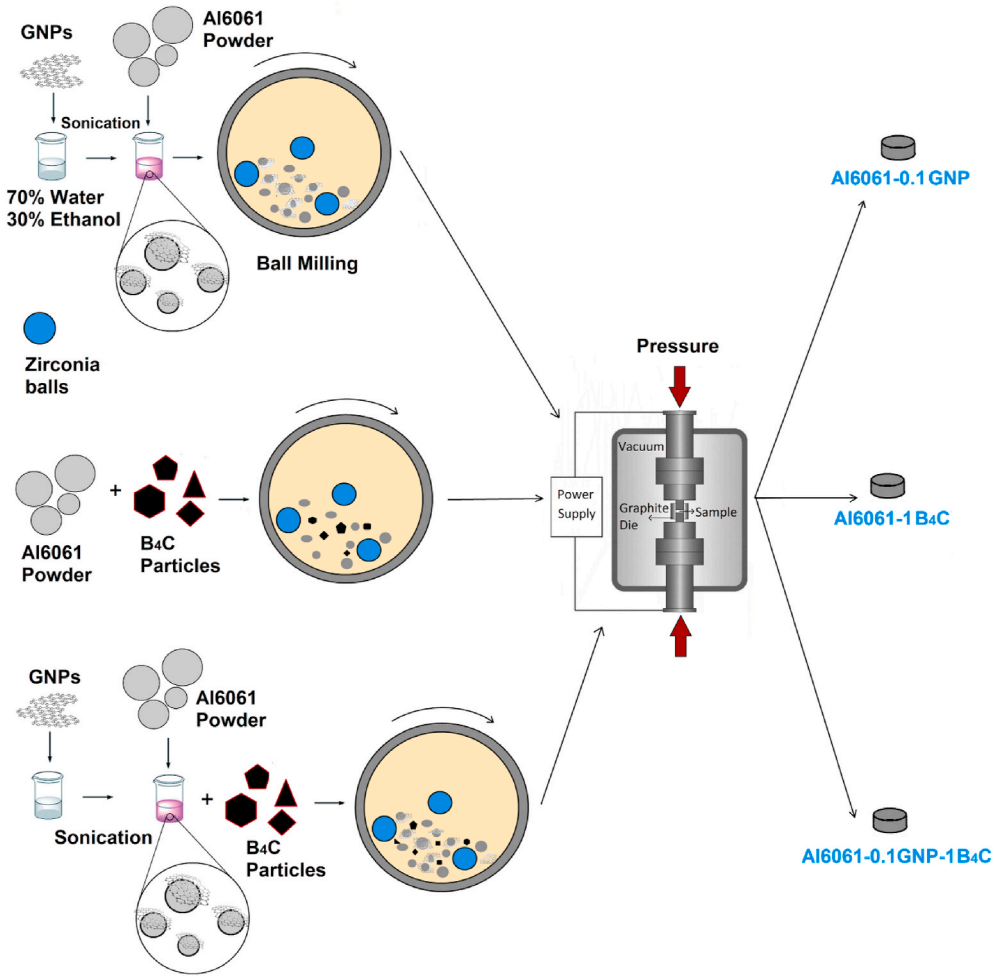

Fig. 2. Schematics of composites processing via ball milling and SPS.

obtain near theoretical densities. Eight samples of each composition were prepared including the reference samples. Four samples were kept in F condition and the other four samples were subjected to T6 thermal treatment by solution treatment at 580 °C for 30 min followed by artificial ageing at 180 °C for 8 h. Nabertherm P 330 was used for the heat treatment. Fig. 2 shows schematics of the process employed for the fabrication of SPSed reference and composite samples.

2.3. Characterization

All the SPSed samples were cut with Struers Silicon Carbide Cut-off wheel 10S15 on Struers Accutom-5. The samples for SEM and OM were mounted in epoxy (EpoFix Hardener 3 parts and EpoFix Resin 25 parts) for grinding and polishing actions. Grinding papers of 500, 800, 1200, 2400 and 4000 grit size were used on Struers RotoPol-31 and RotoForce-4. Struers Tegramin-30 using DiaPro Mol3, DiaPro Nap-B1 and OP-S were used for polishing followed by final polishing on Vibro-Met 2 (Buehler, USA) for 20 h.

EDS was performed on the composite powders and polished SPSed reference and composites using EDAX Octane Pro-A (AMETEK, Inc. USA) installed on SUPRA 55VP. FTIR spectroscopy was performed on the raw materials to explore any detectable attachments and evaluation of the exfoliation process employed for the GNPs. Bruker Vertex 80v was used from 400 to 4000 cm^{-1} data range in transmittance mode at a resolution of 1 cm^{-1}. Raman Spectroscope (Horiba HR800 UV) was used to investigate the existence of GNPs in the ball-milled composite powders. He-Ne-laser of 633 nm wavelength was used at 50 X lens with 600 g/mm grating and data range of 50–3000 cm^{-1}.

Densitometer DH-300 DahoMeter (DogGuan HongTuo Instruments Co. Ltd., China) was used to measure the SPSed reference and composites densities based on Archimedes principle. The raw materials, ball-milled composite powders and the SPSed composites were examined for morphology, dispersion and microstructural evolution with TESCAN MIRA3 field emission SEM. Optical microstructures were investigated using Zeiss AXIO Scope.A1 polarizing microscope after etching by Keller's reagent (2 ml HF, 5 ml HNO_3, 3 ml HCl and 150 ml distilled water). The fractured surfaces of the SPSed reference and composite samples after tensile tests were examined by Zeiss Supra 55VP.

XRD was performed to detect and measure crystallographic changes in the reference and composite samples. DaVinci Bruker D8 Advance, X-Ray Diffractometer was used with scanning angle from 10 to 80° @ 0.2° resolution. EBSD was performed to reveal the grain size, grain boundaries and phase identification for quantitative microstructural evaluation. The samples were subjected to ion beam milling on Hitachi IM-3000 (Hitachi High-Technologies Corporation, Tokyo, Japan) before EBSD. The samples were plasma cleaned in Fischione Plasma Cleaner 1020 (E A. Fischione Instruments, Inc., USA) and were mounted on a copper fixture so that they can be tilted to 70°. Zeiss Ultra 55 was used for the EBSD investigation.

Mechanical characterization was carried out by conducting the hardness and tensile tests. The hardness of the SPSed reference and composites was measured on Shimadzu HMV-G 21DT (Shimadzu, Kyoto Japan) at a test load of 490.3 mN (HV 0.05) and dwell time of 5 s. The tensile test was carried out on Zwick/Roell Z2.5 (ZwickRoell GmbH & Co. KG, Germany) with test sample dimensions of 11 × 1.2 × 3.1 mm (±0.2 × 0.05 × 0.05 mm).

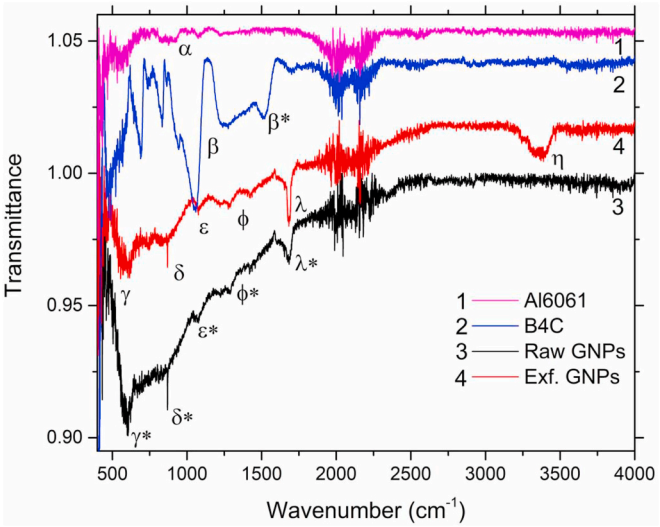

Fig. 3. FTIR of the raw materials used for the fabrication of Al-GNP-B_4C composite (peaks labels are explained in the text); 1) Al6061 powders, 2) B_4C particles, 3) Raw GNPs and 4) exfoliated GNPs after solution treatment.

3. Results and discussion

3.1. FTIR spectroscopy

Fig. 3 shows FTIR transmission spectra of raw materials; Al-6061, B_4C and GNPs in ATR mode. Spectrum 1 shows a shallow band from 811 cm^{-1} to 930 cm^{-1} (α) which can be associated with Al–O–Al bonds of anhydrous Al_2O_3 as reported by F. Fondeur et al. [45]. FTIR of B_4C particles is shown in Spectrum 2, exhibiting characteristics absorption peaks at 1059 and 1520 cm^{-1} (β). These peaks correspond to B–B and C–B bonds, respectively [46,47]. A shallow peak at 1271 cm^{-1} (β*)can be associated with B–O vibrations as reported by M. W. Mortensen et al. [48].

As received GNPs are shown in Spectrum 3 and solution sonicated GNPs are shown in Spectrum 4, respectively. A relatively strong peak could be seen in the fingerprint region around 605 cm^{-1} (γ & γ*) in both raw and exfoliated GNPs arising from impurities associated with graphite precursor [49]. The shallower intensity in Spectrum 4 can be related to the removal of some impurities due to the sonication in the 70/30 water/ethanol mixture. The decrease in impurities related to FTIR peak is due to exfoliation employed by the sonication and this is per earlier studies of Z. Çiplak et al. and D. He et al. [50,51]. Peaks at wavenumber 869 cm^{-1} (δ & δ*) in Spectra 3 and 4 represent the bending vibrations of the C–H bond. A sharp peak of hydroxyl groups (C–O (alkoxy)) stretching vibration at 1078 cm^{-1} (ε & ε*) is also reported by Jaworski et al. [52]. Further analysis of FTIR Spectra 3 and 4, showed peaks at ~1288 cm^{-1} and 1425 cm^{-1} (φ & φ*). Both peaks at respective wavenumber are associated with C–O–C stretching and in-plane bending vibrations of O–H deformation [51].

The stretching vibrations of sp^2 C═C bonds peak which is specific to the asymmetric graphitic carbon in GNPs appeared at 1688 cm^{-1} (λ & λ*) [53] in Spectrum 3. However, the same peak appeared at 1682 cm^{-1} with a stronger intensity in exfoliated GNPs (Spectrum 4). This behaviour can be associated with graphitic carbon atoms interact with the incident beam, more openly and actively owing to the exfoliation process adopted for the GNPs. The slight shift of C═C double covalent bond peak to a lower wavenumber from 1688 cm^{-1} to 1682 cm^{-1} has also been reported by Y. Gao et al. [54]. Raw GNPs showed no attachment of any functional groups. It can also be inferred that absorption bands in such condition may be below the detection limit of the FTIR [55]. However, the presence of a broad signal in the range of 3230–3480 cm^{-1} (η) [50] can be assigned to the O–H stretching. This wide infrared absorption hump can be associated with water absorption during the exfoliation process [49].

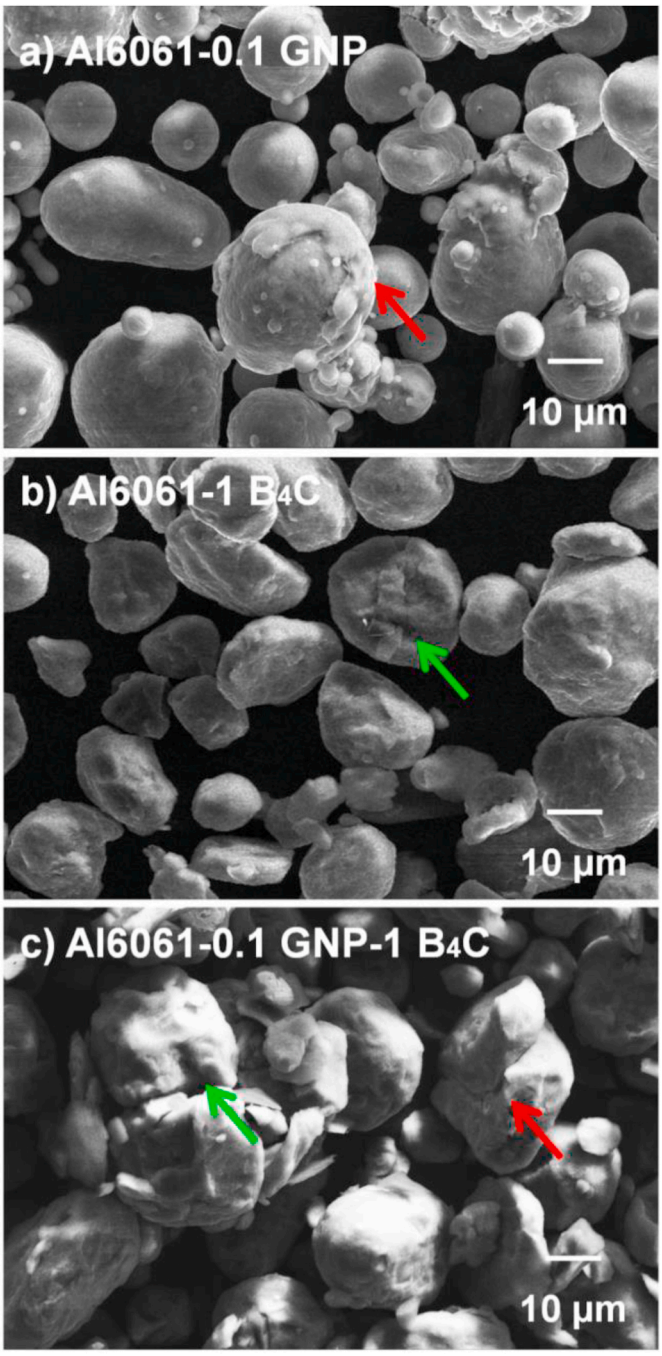

Fig. 4. SEM images of the ball-milled composite powders of (a) Al6061–0.1 GNP, (b) Al6061-1 B_4C, and (c) Al6061–0.1 GNP-1 B_4C.

3.2. Composite powders

Fig. 4 shows, the SEM images of the composite powders after to ball milling operation. Tracing the GNPs in low fraction content is merely impossible due to certain facts; 1) exfoliation of the GNPs during solution sonication and ball milling, 2) uniform distribution of the GNPs in Al6061 matrix and 3) the GNPs are inherently transparent. Mechanically alloyed Al6061 particles can be seen in the referred figure, as marked with a red arrow, possibly with entrapped GNPs as shown in Fig. 4a. Fig. 4b shows Al6061-1 B_4C composite powders after ball milling.

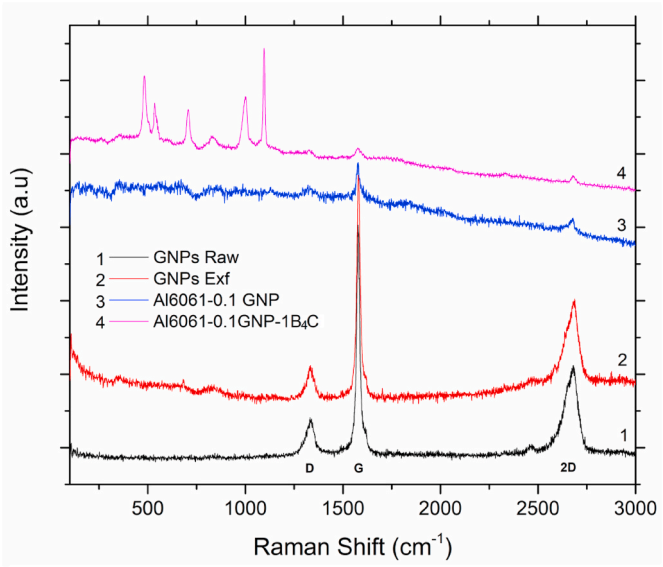

Fig. 5. Raman spectra of; 1) Raw GNPs (as received), 2) solution treated GNPs, 3) ball-milled Al6061–0.1 GNPs powder and 4) ball-milled Al6061-1 B_4C powder.

Table 2
Table showing data extracted from the Raman spectra of GNPs and composite powders.

Sample	I_D/I_G	I_G/I_{2D}	I_{2D}/I_G	w_D (cm^{-1})	w_G (cm^{-1})	w_{2D} (cm^{-1})
As received GNPs	0.11	3.33	0.32	1332.4	1580.5	2685.2
Exfoliated GNPs	0.16	2.78	0.35	1333.5	1578.5	2683.6
Al6061-0.1GNP	0.31	2.35	0.44	1320.7	1578.6	2678.8
Al6061–0.1 GNP-1B_4C	0.42	1.8	0.55	1325	1579	2578

Comparatively, the higher degree of particles deformation, wear and tear marks (marked with a green arrow in Fig. 4b) can be witnessed, as compared to Al6061–0.1 GNPs composite powder (Fig. 4a). Al6061 matrix particles can be identified by sharp cutting edges of B_4C particles marked with a green arrow in Fig. 4b and c. These ridges are responsible for the lesser mechanical alloying of the matrix Al6061 particles.

The Hybrid set of 0.1 wt% GNPs and 1 wt% B_4C in Al6061 matrix is shown in Fig. 4c. The B_4C particles impingement dominated the composite powders by causing severe damage and wear marks on the Al6061 matrix (red and green arrows in Fig. 4c). This wear and tear combined with the mechanical alloying can be related to the higher content of B_4C particles i.e. 1 wt%, causing the GNPs to be trapped in between the Al6061 matrix particles.

3.3. Raman spectroscopy

Raman spectroscopy is among the most powerful tool for the determination of the structure and quality of graphene and graphitic materials. GNPs are the fundamental building block of graphite and carbon nanotubes. Fig. 5, shows the Raman spectra of raw GNPs, exfoliated GNPs, Al6061-0.1GNP and Al6061-0.1GNP-1B_4C composite powders. The Objective of Raman investigation is to examine the survivability of GNPs in the Al6061 matrix after ball milling and SPS operations. The Raman spectra of B_4C contains many characteristic peaks [56] which could mask the GNPs related peaks at the specific wavenumbers. Table 2 shown the intensity ratios of the raw GNPs, exfoliated GNPs, Al6061-0.1GNP and Al6061-0.1GNP-1B_4C composite powders. The G and D band intensities and positions relate to the graphitic bonding and defects/impurities are shown in Fig. 5. The presence of these GNPs

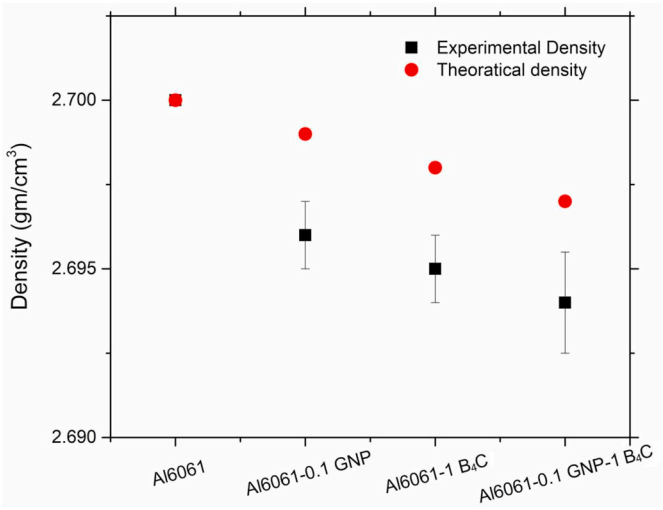

Fig. 6. Density curves with wt.% of reinforcements for the reference, Al6061–0.1 GNP, Al6061-1 B_4C and hybrid Al6061–0.1 GNP-1 B_4C composites.

characteristic peaks, verify the survivability and retention of GNPs in the Al6061 matrix after solution treatment and ball milling operations.

The appearance of a very sharp and distinct G-peak (1580.5 cm^{-1}) and a lower intensity D-peak (1332.4 cm^{-1}), asserts the presence of few layers of GNPs in as-received condition, as shown in Spectrum 1 of Fig. 5. A shift to lower wavenumber in Spectrum 2 is observed with an increase in the I_D/I_G ratio representing delayering of the GNPs. This trend conforms to the earlier studies of X. C. Wei et al. [57] and C. Damm et al. [58]. The success of employed solution sonication can be verified in the light of available studies. A drastic decrease in the intensity of the G band can be witnessed due to a lower GNPs wt.% and higher Al6061 matrix. The metallic matrix particles attenuate the incident laser to a greater extent, compared to the monolithic GNPs. Change in the I_D/I_G ratio (Table 2) reflects the presence of strains. These strains are caused by delayering of the GNPs layers, causing bending and increase of interlayer distance.

Earlier studies on the exfoliation of graphene by A. Hadi et al. [49] and X. Cai et al. [59] confirm the results of the present study. The strains accumulated during the ball milling process in the presence of Al6061 particles, affect the C–C bond length and distort the symmetry of hexagonal carbon atoms. This is evident from the increase in I_D/I_G ratio. The evidence is also reported in the earlier study [60] (Spectrum 3, Fig. 5). Another confirmation comes from the shift of G-band peak position (w_G) which shifts to a lower wavenumber. The shift of G-band to lower wavenumber is due to vibrational frequency, reported by Z. W. Zhang et al. [61]. Thus the exfoliation of the GNPs is caused by the strains introduced by the ball milling process. The comparatively smaller and broader 2D peaks represent the GNPs thickness. The broadening of w_{2D} and shift to a lower wavenumber shows a decrease in convoluted graphene layers bands [38]. This reduction in the intensity of the 2D peak is a function of the ball milling operation and an indication of the amorphous GNPs. This amorphization is a measure of the disorder in GNPs structures due to the milling operation.

Spectrum 4 shows the Raman spectra of hybrid ball milled composite powders, i.e. Al6061-0.1GNP-1B_4C. The GNPs specific D, G and 2D peaks have diminished to a greater extent in the presence of B_4C specific peaks at 486, 533, 700, 833, 1000 and 1095 cm^{-1}. These peaks are in accordance with the earlier studies by K. M. Reddy et al. [56] and G. Victor et al. [62]. The decreasing I_G/I_{2D} ratio of the Al6061-0.1GNP-1B_4C composite powder shows an increase in the defective GNPs structure, which can be related to the GNPs slithering [63].

Table 3
Densities of the reference and SPSed composites.

Description	Theoretical Density (gm/cm^3)	Experimental Density (gm/cm^3)
Ref. Al6061	2.7	2.7 ± 0.0
Al6061–0.1 GNP	2.699	2.696 ± 0.001
Al6061-1 B_4C	2.698	2.695 ± 0.002
Al6061–0.1 GNP-1 B_4C	2.697	2.694 ± 0.002

3.4. Composites densities

Theoretical densities of the reference and SPSed composite samples were calculated by the rule of mixture, as given by equation (1) [64];

$$\rho_c = \rho_G V_G + \rho_M V_M + \rho_B V_B \quad (1)$$

where, "ρ" is the density and "V" is the volume fraction and the subscripts "c", "G", "M" and "B" symbolize the composite, GNPs, Al6061 matrix and B_4C respectively. The experimental densities of the reference and SPSed composites were measured by the Archimedes method. Fig. 6 shows the density curves of the reference and the respective reinforcement contents in the Al6061 matrix. The addition of lower density reinforcements in the matrix results in a decrement in bulk density, as compared to the monolithic/unreinforced Al6061 matrix.

Table 3 shows densities of the reference and SPSed composites. Density measurements of four samples were made, likewise; two in F condition and two in the T6 condition. Authors have reported in a study on Al-GNPs composites that the T6 condition does not affect the bulk composite density [43]. The GNPs and B_4C, being lighter (~2 and 2.5 gm/cm^3, respectively) than the Al6061 matrix (2.7 gm/cm^3) tends to reduce the bulk density of the final composites. The choice of processing method greatly influences the density of the final composite [65]. Fig. 6 shows the comparison of theoretical densities with the experimentally measured densities. Metallic densities of the reference samples in F and T6 conditions are as per the reported values by J. Campbell [66].

The decrease in density with the addition of GNPs can also be associated with the difference in melting points of the Al6061 matrix and GNPs (660 °C and ~4625 °C, respectively). Thus causing a non-wetting tendency at the mating surfaces of the GNPs/Al6061 interface. The possibility of interlayer pores within GNPs may arise resulting in an overall decrease in the experimental density compared to the theoretical value [18]. SPS is a well-reputed processing technique in terms of achieving near theoretical densities in the final product [17]. B_4C particles in micron size, offer a higher void content due to the change in morphology and shape when compared to the Al6061 matrix particles' profile. The results shown in Fig. 6 are in accordance with the earlier study by Antadze et al. [67]. The hybrid composite displayed a decrease in the density, owing to higher wt.% of both reinforcements (GNPs and B_4C) in the Al6061 matrix. The adhered GNPs on the Al6061 particles shields the grains from an impingement of B_4C particles and fuse in during the SPS sintering. This effect can be related to the addition of voids, comparatively higher than solely reinforced GNPs and B_4C SPSed composites, thus resulting in the lowest composite density.

3.5. Microstructure evolution

3.5.1. Optical microscopy

Optical micrographs of the reference and SPSed composites (as per Table 1c) are shown in Fig. 7. The microstructure analysis is carried out to investigate the densification and extent of sintering of ball-milled powders. The microstructures show near theoretical densification of the SPSed reference and the composites without any indications of porosity. The microstructures reveal sintered morphology of the grains and the bonding of aluminium powders after SPS. Intense plastic deformation owing to the cold compaction and SPS sintering resulted in microstructural changes.

The reference samples' microstructure in T6 is shown in Fig. 7a. The artificial age hardening T6 process was controlled in such a way that no grain growth could take place, therefore any deviation from the fabricated (F) grain size is not observed. The GNPs are optically transparent and cannot be observed under light microscopy on any polished and

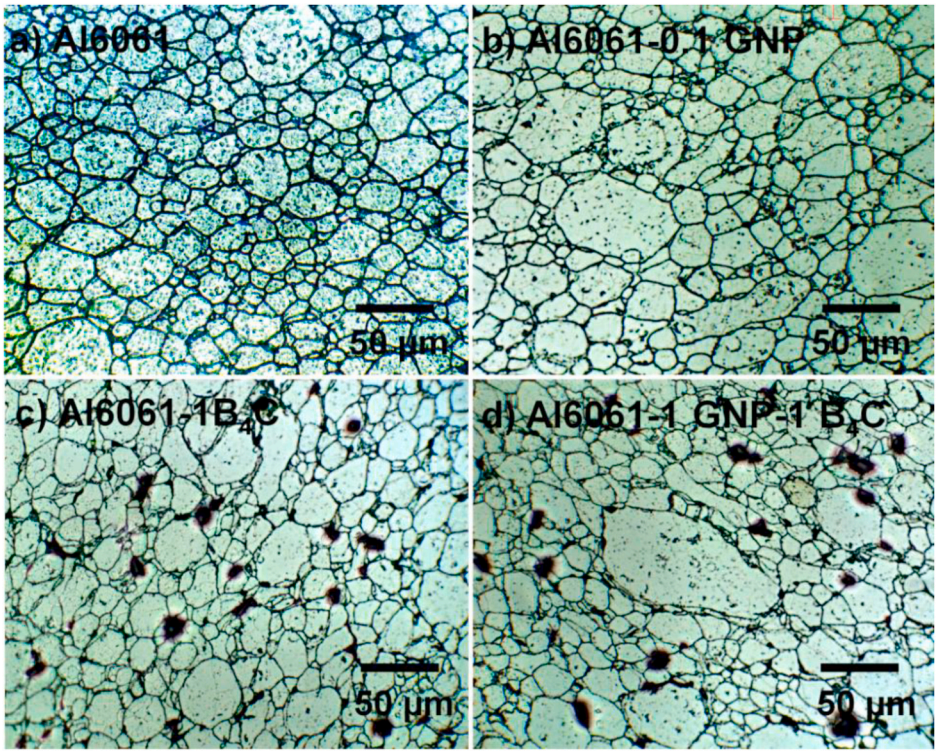

Fig. 7. Optical micrographs of a) reference sample in T6, (b) Al6061–0.1 GNP-T6, (c) Al6061-1 B_4C-T6, and (d) Al6061-1 GNP-1 B_4C-T6 composites.

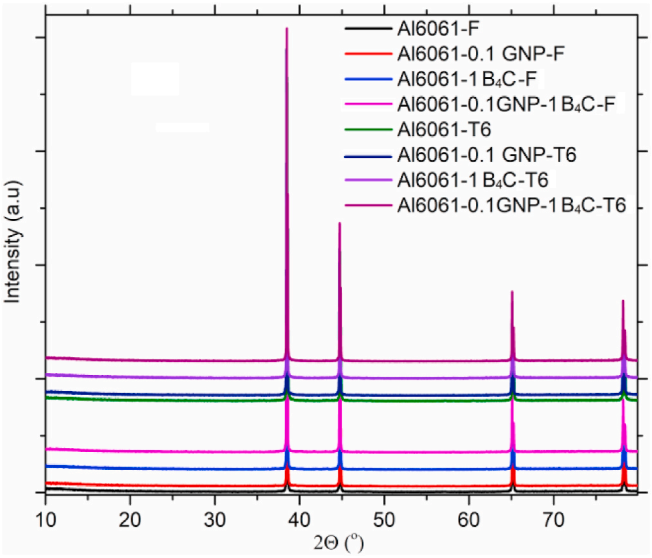

Fig. 8. XRD patterns of the SPSed reference and all the composites in F and T6 conditions.

etched surface [1]. However, the agglomerated GNPs or lumped GNPs appear as dark spots or lines [68]. The GNPs are present at the grain boundaries, practically entrapping the distorted and sintered Al6061 matrix grains [43]. A decrease in the grain size can be perceived in the presence of GNPs, which is later evaluated by EBSD in this study. This observation is in agreement with the study of Saboori et al. [69]. Fig. 7b shows the Al6061-0.1GNP composite in the T6 condition. No prominent agglomeration or lumps of GNPs can be noticed at this magnification. Based on this observation, it can be inferred that the non-visible GNPs did not form lumps that could be visible and the well-dispersed GNPs resulted in a uniform distribution in the Al6061 matrix at the selected ball milling processing conditions [33].

The addition of B_4C (dark phase) in the Al6061 matrix is primarily investigated for the distribution in the Al6061 matrix (bright phase) due to their distinct appearance. The microstructure of Al6061–1B_4C composites in T6 is shown in Fig. 7c. The polished and etched surface shows, uniform distribution of B_4C particles in the Al6061 matrix. Chemically dissimilar B_4C particles are accommodated at the grain boundaries of the Al6061 matrix. These particles act as nails embedded in the continuous phase of the matrix (bright phase). These impinged B_4C particles cause interlocked hinges at the matrix grains boundaries [70]. Thus resulting in enhanced mechanical strength, discussed later in detail. The SPS processing variables and lower exposure time do not allow the formation of any intermetallic phase like alumino-borocarbide, as reported by the authors in their earlier work [2].

Fig. 7d shows the microstructure of the hybrid SPSed (Al6061-0.1GNP-1B_4C) composite in the T6 condition. The enwrapped GNPs, mask B_4C particles by mechanically alloyed with the Al6061 matrix. Uniform distribution of the GNPs and B_4C particles can be seen as in the microstructures of the Al6061-0.1GNP-1B_4C composite. Predominantly, a two-colour contrast in the microstructure shows no potential existence of any third phase formation during the SPS processing. However, the XRD results would be discussed in detail for the detection of any possible phase or interface at the reinforcement-matrix interface.

3.5.2. XRD

XRD of all the SPSed samples (as per Table 1c) are shown in Fig. 8. Typical peaks corresponding to aluminium [71] can be seen at the respective plane positions ($2\theta = 38.4°$). The intensity of the (111) plane remains, as the maximum contributor of X-ray diffraction for the reference and all the SPSed composites. Other characteristic XRD peaks

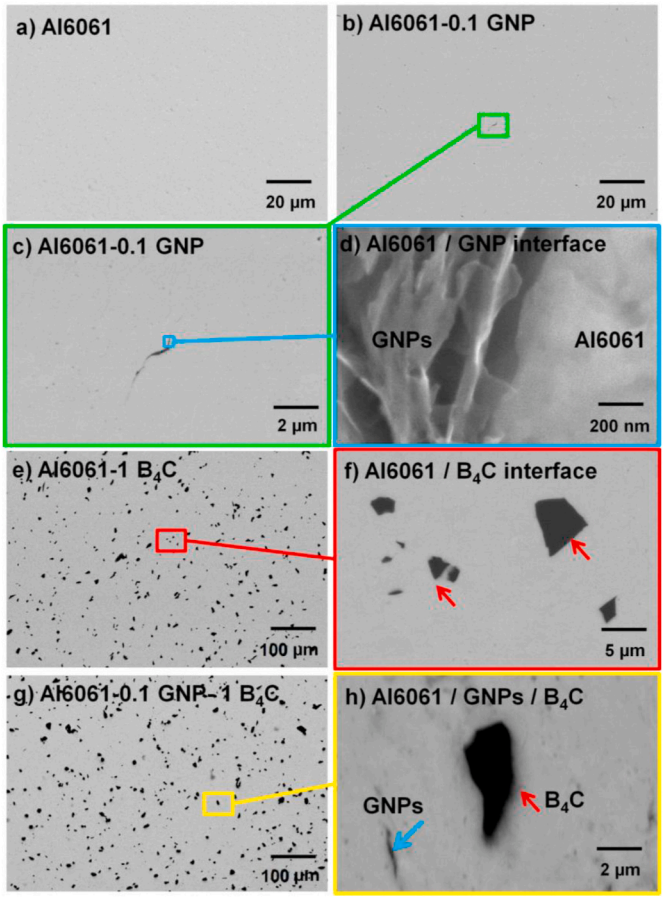

Fig. 9. SEM images of; a) Al6061 reference, b) Al6061–0.1 GNP composite, c) GNPs lump magnified in Al6061–0.1 GNP, d) Al6061/GNPs interface, e) Al6061-1 B_4C composite at low magnification, f) higher magnification in Al6061-1 B_4C composite, g) Al6061–0.1 GNP-1 B_4C composite at low magnification, and h) interface of Al60061/B_4C/GNPs interface.

of aluminium at their respective crystallographic planes can be seen (2θ [200] = 44.7°, 2θ[220] = 65.1°, 2θ[331] = 78.2°) in Fig. 8. No peaks related to the GNPs could be seen in the Al6061-0.1GNPs composite, as the same has been reported by W. M. Tian et al. [72]. The detection limit of the XRD diffractometer can be the possible reason for not detecting GNPs in 0.1 wt% addition. An earlier study by M. Bastros et al. presented the same detection limit of XRD [38]. On this basis, the existence/formation of aluminium carbide (Al_4C_3) at $2\theta = 55°$ can be ruled out. SPS processing is unique due to its minimum sintering time at high temperatures. Whereas the formation of Al_4C_3 is reported at higher temperatures and under pressure along as presented by L. A. Yolshina et al. [9] for hot-pressing. The characteristic peaks of B_4C at 2θ positions; 19.6° 5, 21.9°, 23.4°, 34.8° and 37.6°, were not detectable owing to the same reason as discussed for GNPs in the Al6061 matrix.

3.5.3. SEM

SEM images of the polished unetched surfaces of the reference and composites in secondary electron mode are shown in Fig. 9. Grain boundaries are invisible due to unetched surfaces, therefore SEM analysis is carried out to investigate the reinforcement distribution and interfacial characterization, despite thermal condition (F or T6) as represented by Fig. 9a. No significant pores were observed at the said resolution. The SEM observations can be correlated to the near theoretical densification of the SPSed reference and composite samples. The GNPs are expected to surround the Al6061 grains, in other words, an anchoring effect can be assumed. Fig. 9b and c shows a rarely encountered GNPs' lump interlocked between matrix grains in Al6061–0.1 GNP

Table 4
EBSD data extracted for microstructural comparison.

Description	Avg. Grain Diameter (μm)	ASTM (#)	Grain/ mm (#)	Misorientation (°)
Al6061–F	12.44	9.36	80.4	24.54
Al6061-T6	12.41	9.37	80.5	24.56
Al6061–0.1 GNP-F	11.93	9.48	83.8	27.95
Al6061–0.1 GNP-T6	11.87	9.5	84.3	28.08
Al6061-1 B_4C–F	11.86	9.5	84.3	26.32
Al6061-1 B_4C-T6	11.79	9.52	84.8	27.42
Al6061–0.1 GNP-1 B_4C–F	11.70	9.54	85.5	28.48
Al6061–0.1 GNP-1 B_4C-T6	11.69	9.54	85.5	28.58

composite. A neat and clean interface, free from any interphase can be seen in Fig. 9d. This strengthens the XRD results already discussed.

The microstructure evolution of the Al-GNPs composites is greatly influenced by the grain size, GNPs distribution, recrystallization temperature and plasticity of the matrix during consolidation processes [73]. Generally, the decrease in grain size can be related to the uniform distribution of GNPs in the Al6061 matrix [74]. The input of deformation energy from the ball milling results in mechanical alloying or cold welding of the matrix particles with each other and GNPs. Thus, the entrapped GNPs can be assumed to be interlocked in the Al6061 matrix grains, causing an anchoring effect, which is further investigated in the subsequent section of fractography.

Fig. 9e shows, Al–B_4C composite in 1 wt% loading. No significant pores or cavities can be seen, in general, therefore augmenting the claim of fully dense SPSed composites. No agglomeration of the B_4C particles can be seen owing to their uniform dispersion in the Al6061 matrix at the selected ball milling parameters [75]. At higher magnification, Fig. 9f shows B_4C particles embedded in the matrix with a neat and clean Al6061/B_4C interface. The hybrid composite Al6061–0.1 GNP-1 B_4C (Fig. 9g and h) showed a similar appearance as Fig. 9e. The GNPs being optical transparent are absent in the SEM view, as the B_4C dominates the hybrid composite microstructures, No isolated clusters or distinguishable GNPs lumps could be seen in Fig. 9g, except for the discrete suspected rarely encountered GNPs marked with a blue arrow in Fig. 9h. No evidence of an interphase or colour contrast at the interface of matrix/reinforcement could be witnessed.

3.5.4. EBSD

EBSD is a powerful tool for microstructural studies based on the crystallographic characterisation of aluminium alloys [76]. EBSD data greatly depends on the Confidence Index (CI) which is a measure of matching the Kikuchi patterns of the test specimens with the database aluminium. The Kikuchi patterns matching by the software is based on the Hough method [77]. Table 4 summarises the EBSD data and corresponding CI of the reference and SPSed composites. The pattern matching solely depends on the surface finish despite other instrumental factors. Keeping the same surface preparation/metallographic conditions for all the samples, the decrease in CI reveals the fact that reinforcements are present in the Al6061 matrix which eventually affects the EBSD data. All the SPSed samples were prepared with the same grinding/polishing parameters; therefore changes in CI are directly related to the extent of reinforcements and the associated changes in the microstructure.

Fig. 10 show the reference sample exhibited a CI of 0.97, owing to the flat and reinforcement free plane surface (Fig. 10a). The addition of B_4C in 1 wt% lower the CI to a value of 0.83 (Fig. 10b). The reason behind this decrease in CI is difficulty in grinding polishing of B_4C particles embedded in a matrix, as the hard B_4C particles offer resistance in polishing operations compared to unreinforced Al6061 matrix grains. Thus, the partially uneven surface affects the EBSD pattern matching.

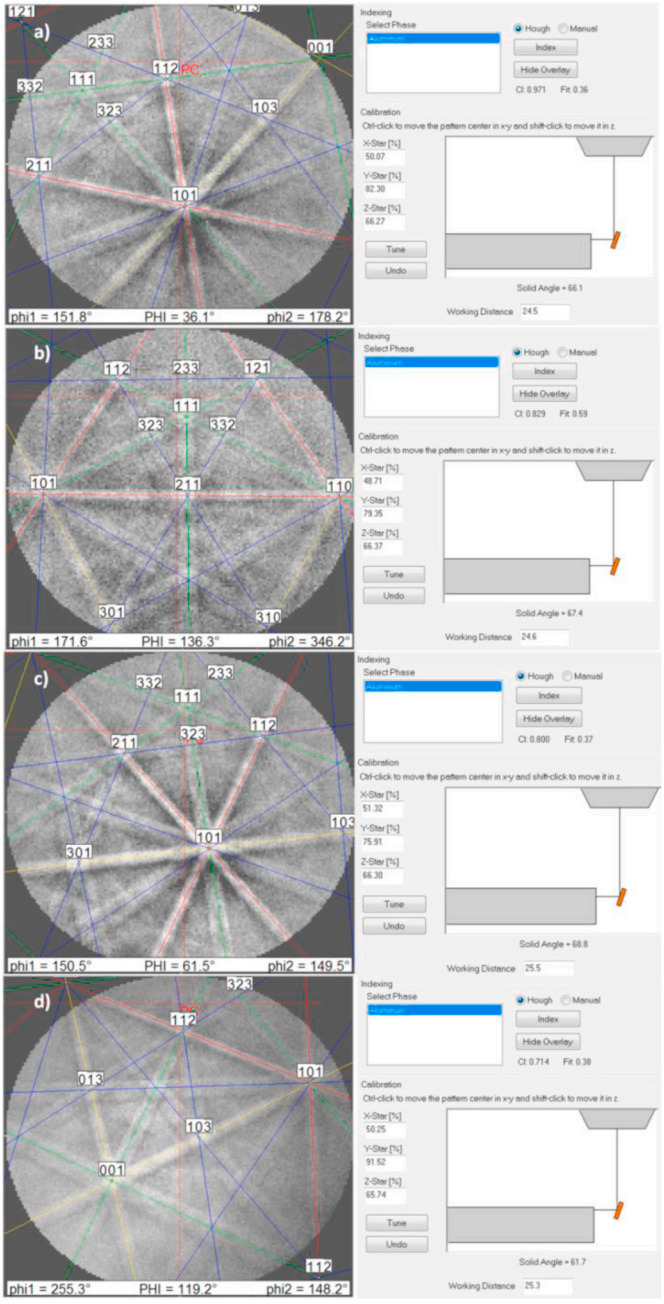

Fig. 10. EBSD pattern matching with CI values and axis parameters for a) reference Al6061, b) Al6061-1 B_4C, c) Al6061–0.1 GNP and d) Al6061–0.1 GNP-1 B_4C composites.

However, the value is still higher than other reported study [78]. Being thin sheets of carbon atoms with lengths in microns, the effect of GNPs on the surface finish of the Al6061-0.1GNPs composites is lesser than discrete B_4C particles [43]. However, compared to the discrete size of the B_4C particles, GNPs spread more widely along the grain boundaries due to their higher surface area. Therefore the infinitesimal difference was observed in the value of CI. Fig. 10c shows the pattern matched at a CI of 0.80. These values are sufficiently suitable for the interpretation of grains and associated details. The hybrid composite of 0.1 wt% GNPs and 1 wt% B_4C matched the reference pattern with a CI of 71%, as can be seen from Fig. 10d. The combined effect of both reinforcements decreased the CI to slightly lower but still acceptable value.

The inverse pole figures (IPF) of Al6061 reference samples in F & T6 condition along with other SPSed composites are shown in Figs. 11 and

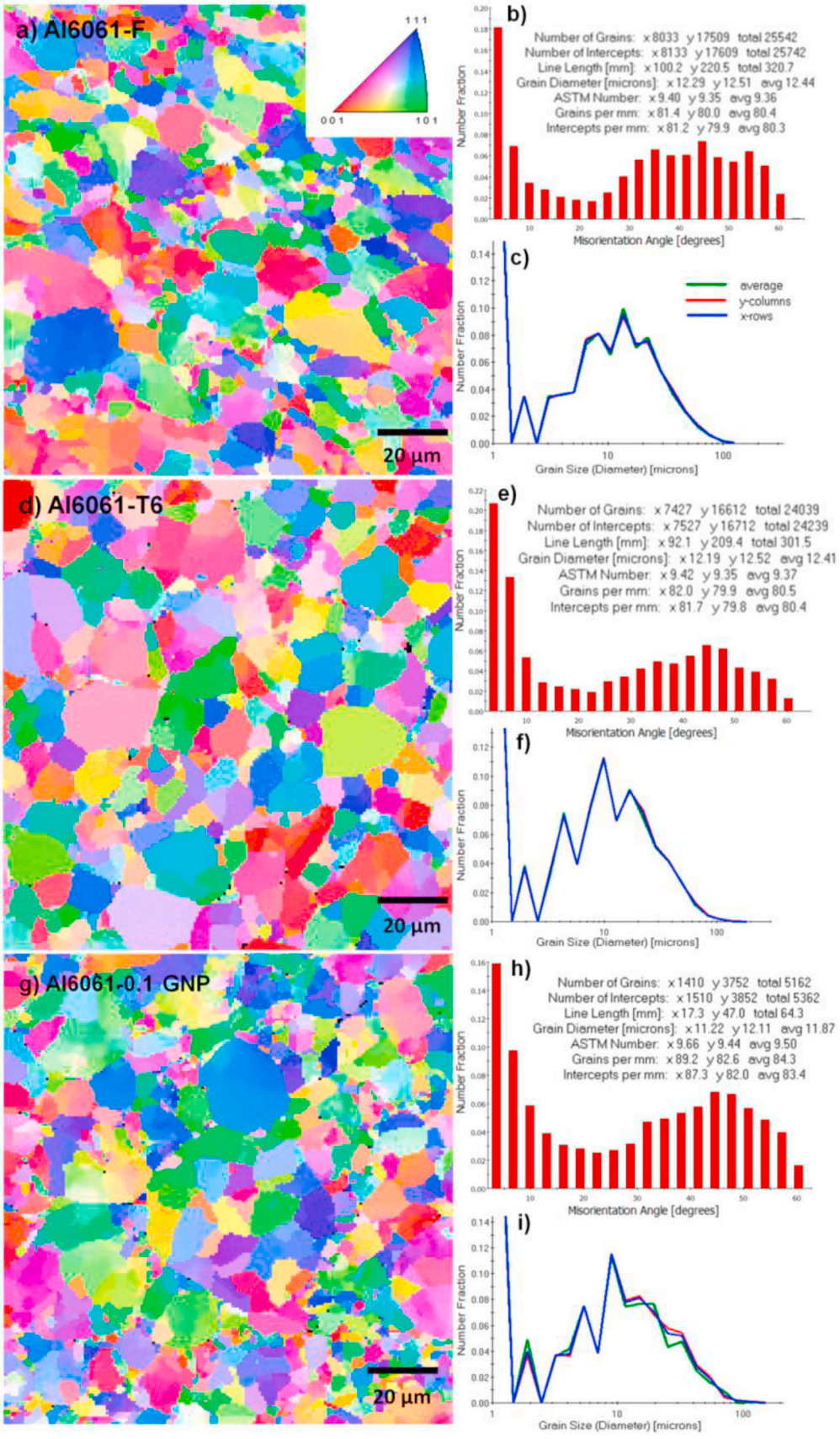

Fig. 11. IPF images of a) reference Al6061 sample in F, b) EBSD data and area fraction plotted with the misorientation angles, c) grains measurement data, d) Al6061-T6, e) misorientation data, f) grains data for Al6061-T6, g) Al6061–0.1 GNP, h) misorientation data, and i) grains size plot.

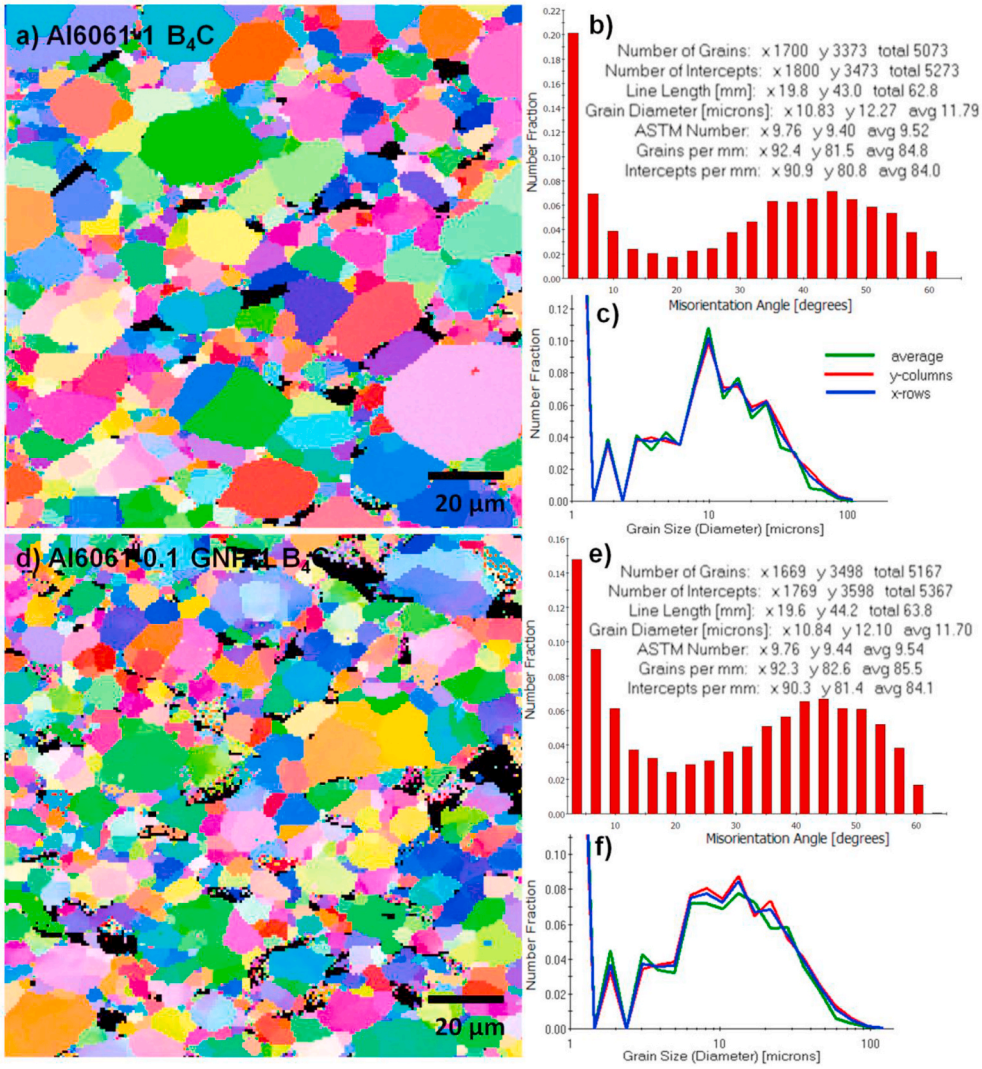

Fig. 12. EBSD data of a) Al6061-1 B_4C composite, b) graph showing misorientation measured from IPF, c) grain size measurement plot, d) Al6061–0.1 GNP-1 B_4C composite, e) misorientation plot with area fraction, f) grains size measurement plot.

12. No difference in the F and T6 was observed. The basis laid down in selecting either of the thermal conditions for grains data proves valid in EBSD. The IPF revealed almost similar grains data for the remaining composite compositions in either F or T6. Table 4 shows the EBSD data of the reference and SPSed composites in F and T6 conditions. The restricted grain growth was controlled during solution treatment by temperature and time. Therefore, the forthcoming discussion, regarding the EBSD would be generalised to the microstructural evolution despite thermal conditions.

Fig. 11a and d shows the reference Al6061 in F and T6 thermal conditions, respectively. No discrimination could be found based on grains data. Fig. 11g, h and i show IPF images of 0.1 wt% GNPs. The addition of GNPs in the Al6061 matrix resulted in a ~6% reduction in grain size. The results are as per the author's earlier findings on the same raw materials [43]. The wrapping of GNPs around the Al6061 grains restricts grain growth. Similarly, the presence of GNPs has affected the grain misorientation as can be seen in Fig. 14. This phenomenon can be related to the mechanical alloying and entrapment of the GNPs in Al6061 matrix grains. The entrapped GNPs during ball milling and subsequently in SPS results in local strains at the particle/matrix interface. As the sintering proceeds, the entrapped GNPs in-between the matrix particles restrict the alignment and settling of the matrix grains due to the thermal mismatch barrier between, thus hindering the grains orientation and grain boundary matching. The mismatch of Al6061 matrix grain due to entrapped GNPs is higher as compared to the reference samples due to the highest surface area among the selected reinforcements.

Fig. 12a, b and c show the IPF images and data of the Al6061-1 B_4C composite. The un-indexed areas appearing as black spots are B_4C particles. Uniform distribution of B_4C particles can be seen at the said magnification [44,79]. The addition of 1 wt% B_4C particles reduced the grain size of the Al6061 matrix by ~5%. The contributing factors in grain refinement can be linked with a comparison with GNPs reinforced Al6061–0.1 GNP composites; 1) higher B_4C content than GNPs resulting in higher interfacial interaction with Al6061 matrix grains and 2) impingement of B_4C particles causes sharp ridges and edges on the Al6061 grains which restrict grain growth.

The B_4C particles being ceramic and distinct from the Al6061 matrix is generally present at the grain boundaries. These B_4C particles are embedded in Al6061 matrix grains as shown in Fig. 6c and d. It can be noticed that the B_4C particles are surrounded by smaller Al6061 grains. The reasons for this grain refinement can be explained as the larger Al6061 matrix particles are merely impossible to be penetrated by the B_4C particles, thus they are retained at the grain boundaries accompanied by smaller Al6061 matrix particles to accommodate the space. The EBSD (Fig. 14) results show a decrease in the grain size due to B_4C

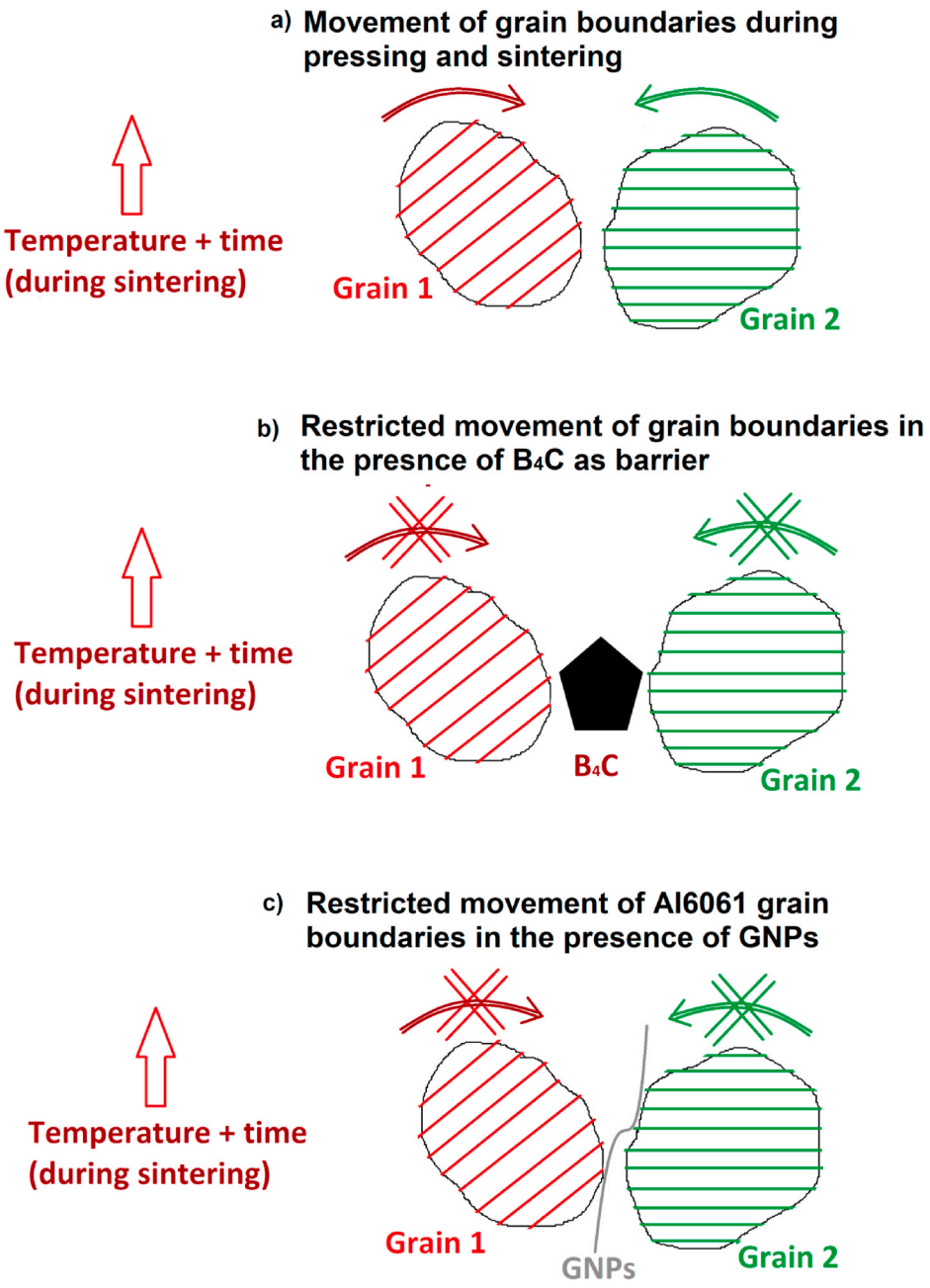

Fig. 13. Model illustration showing the restricted movement of the grain boundaries during pressing and sintering, for a) Al6061 reference sample, b) with B_4C and c) entrapped GNPs.

content. The impingement of B_4C particles on the surface of the Al6061 matrix particles during ball milling results in ridges and sharp cutting edges. These marks reduce the tendency of the grains to growth during SPS sintering.

EBSD grains data of the hybrid SPSed composite is shown in IPF image Fig. 12d. The grain size reduction and misorientation (Fig. 12e and f) added up due to the presence of GNPs and B_4C particles in the Al6061 matrix (Fig. 14). Fig. 13 shows an illustrative model representing the movement of Al6061 grain boundaries during SPS sintering. The time and temperature allow matrix particles to fuse during sintering with relative movement over each other, thus the possibility of matching grains boundaries is highly expected (Fig. 13a). In the presence of GNPs, the adjacent Al6061 matrix grains become blind to each other, thus unable to match the grains sliding/orientation. A similar situation arises in the presence of B_4C particles, as the impinged ends/corners/edges of the B_4C particles restrict the Al6061 matrix grains to adjust and accommodate them for minimum misorientation during sintering (Fig. 13b). However, in the hybrid combination of both reinforcements, the mismatch of grain boundaries angles is the highest. As can be seen from the EBSD results plotted in Fig. 14. The important factor to be noted in grains orientation mismatch is the decrease in Al6061-1 B_4C composite compared to the Al6061-1 GNP composite. The explanatory reason is that the exfoliation of GNPs results in a huge number of graphene layers to cover the Al6061 matrix grains compared to the discrete individual B_4C particles.

3.6. Mechanical characterization

3.6.1. Hardness

Table 5 shows the hardness values of reference samples and SPSed

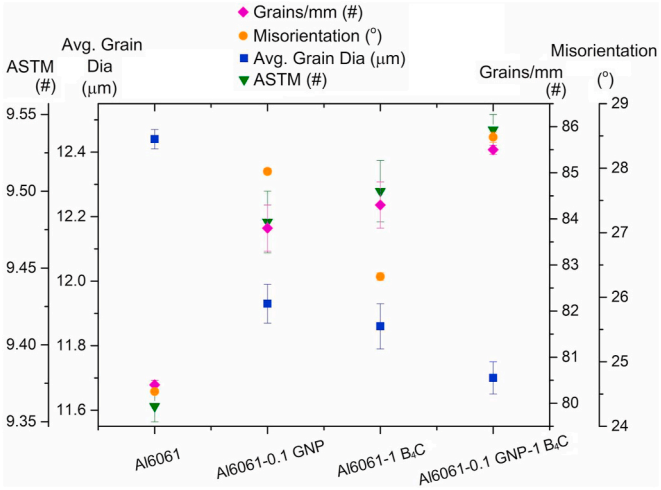

Fig. 14. Plots of grain size, corresponding to the ASTM number, grains/mm and misorientation versus the reinforcement content in Al6061 matrix.

Table 5
Hardness table of reference samples and all the composite groups.

Description	Hardness	Err	Hardness	Err
	F		T6	
	Hv	Hv	Hv	Hv
Al6061	49	± 2	72	± 2
Al6061–0.1 GNP	58	± 2	80	± 2
Al6061-1 B_4C	62	± 4	88	± 4
Al6061–0.1 GNP-1 B_4C	65	± 4	90	± 4

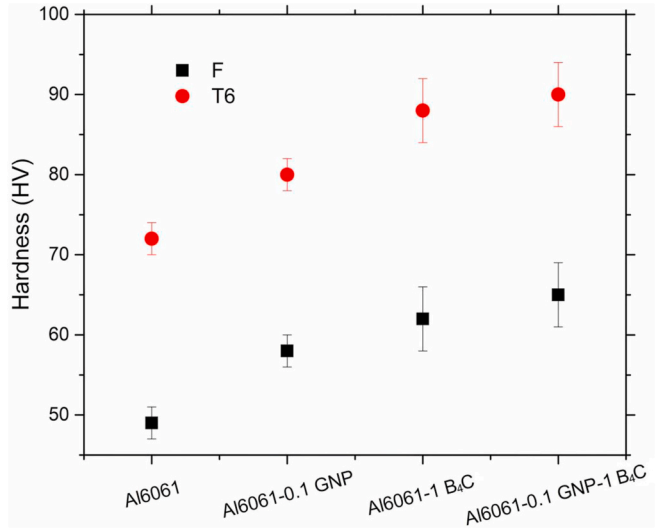

Fig. 15. Graph between Vickers hardness showing variation with GNPs and B_4C content in F and T6 Al6061 matrix.

composites in F and T6 conditions (Fig. 15). On average, five micro indents were made for hardness measurement from each sample. The reference sample exhibited a value of 49 ± 2 HV and 72 ± 2 HV in F and T6 conditions, respectively. The reference T6 is 47% higher than the F sample. Incorporation of 0.1 wt% GNPs in the Al6061 matrix added 18% and 11% increase in the hardness of Al6061 matrix in F and T6, respectively. An incremental increase in the hardness has also been reported by F. H. Latief et al. [80] in pure aluminium due to the addition of GNPs. Similarly, the addition of 1 wt% B_4C particles in F and T6 thermal

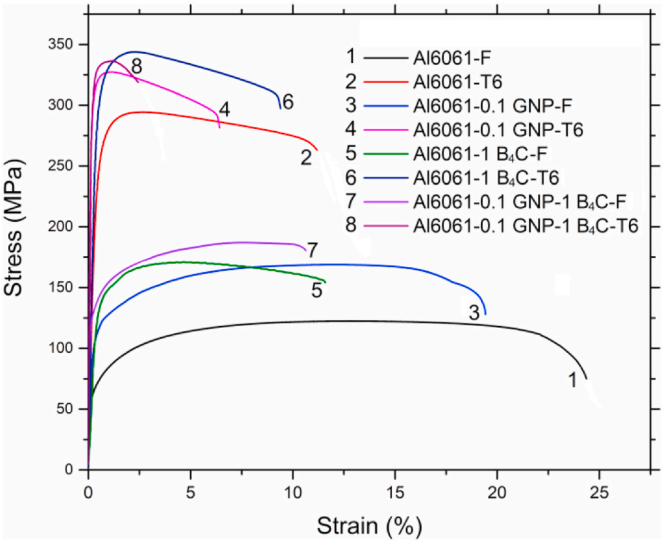

Fig. 16. Tensile testing stress-strain curves of F and T6 reference and Al6061-GNP/B_4C composites.

conditions added 27% and 22% increase in hardness.

A hybrid combination of both reinforcements in the Al6061 matrix resulted in a 33% and 25% increase in the hardness, compared to the reference samples in the same thermal conditions. The increase in hardness can be explained by the concept of thermal mismatch generated by the presence of a second phase in the Al6061 matrix. The second phase stresses the continuous phase by adding dislocations strains fields in the matrix [81], thus generating a nonequilibrium state. The presence of both nano and micro-scale reinforcements adds strains fields in the base metal therefore higher response in hardness of the Al6061 matrix is observed.

An increase in the hardness of hybrid SPSed composite is an indication of an increase in the strength, as show in Fig. 15. Densification and uniform dispersion of GNPs and B_4C are the two contributing factors in the improved hardness of the SPSed composites. The role of GNPs in the hybrid reinforced Al6061 matrix was to surround the matrix grains and restrict the grain growth as evident from the EBSD data (Table 4). An increase in hardness can also be associated with the thermal mismatch of reinforcements with the Al6061 matrix. This strengthening mechanism is explained by V. Sharma et al. [82]. The obvious difference in thermal properties of reinforcements and the Al6061 matrix result in the generation of stresses dispersed all around the matrix. The difference in coefficient of thermal expansion from SPS temperature to the room temperature influences the hardness of the resulting composites.

3.6.2. *Tensile test*

Fig. 16 shows the tensile stress-strain curves of the SPSed reference and all the composites in F and T6 condition. The effect of thermal conditions and reinforcements on the strength and ductility can be seen in Table 6. Five samples of the reference and each composite were tested to ensure representation and reproducibility. An increase in the yield strength and ultimate tensile strength was recorded at the cost of ductility of the samples. The reference samples in F and T6 exhibited baseline values for further comparison with the SPSed composites. The reference SPSed samples revealed yield and tensile strength of 62 ± 3 MPa, 122 ± 4 MPa and 189 ± 4 MPa, 244 ± 3 MPa, respectively. Incorporation of GNP in 0.1 wt% added 61% yield strength and 30% tensile strength at the cost of a 24% decrease in the ductility of Al6061 matrix in F condition. Whereas in the T6 condition the contribution of GNPs is 23% and 8% in yield and tensile strength. A drastic decrease of 50% was measured in the T6 thermal condition. Besides the increase in tensile strength of Al6061–0.1 GNP composites, an evident decrease in

Table 6
Tensile test data exacted for quantitative comparison of reference and SPS composites in fabricated and T6 conditions.

Description	YS	Err	TS	Err	FS	Err	YS	Err	TS	Err	FS	Err
	MPa	MPa	MPa	MPa	%	%	MPa	MPa	MPa	MPa	%	%
	F						T6					
Al6061	62	±3	122	±4	25	±2	189	±4	244	±3	12	±1.5
Al6061–0.1 GNP	100	±3	158	±4	19	±1	233	±4	263	±3	9	±1
Al6061–1 B_4C	118	±4	171	±5	11	±1.5	240	±4	280	±4	7.2	±1
Al6061–0.1 GNP-1 B_4C	122	±4	182	±4	9.8	±1	252	±5	292	±3	2.4	±0.5

the contribution of GNPs in the T6 matrix can be witnessed (Fig. 16). An increase in the tensile strength due to the addition of GNPs is higher in the F condition compared to the T6 condition. Lesser load transfer capability of the T6 matrix due to higher hardness and internal resistance to deformation is the main reason for this poorer contribution of GNPs.

The addition of 1 wt% B_4C particles in the Al6061 matrix demonstrated an increase in the yield and tensile strength in F and T6 conditions. Fig. 17 shows the tensile properties for the reference and SPSed composites with respective reinforcement's content. The presence of B_4C in the matrix results in higher impingement on the grain boundaries and thus higher dislocation density causes severe strain hardening [17]. An increase of 90% in the yield strength (Fig. 17a) is recorded at the cost of a 56% decrease in the failure strain in the F condition. The T6 composites of the same composition demonstrated a 27% increase in yield strength and 15% in tensile strength, compared to the T6 reference standard of Al6061 reference (Fig. 17b). A decrease of 58% failure strain is recorded for the Al6061-1 B_4C composites in T6 thermal condition (Fig. 17c). Impingement of B_4C particles causes severe damage during ball milling on the Al6061 matrix. These deformed strained grain boundaries are sintered under pressure during SPS. The increase of tensile properties is related to the presence of B_4C particles and associated stresses induced during the ball milling process. The T6 composites are strengthened by the precipitation of Mg_2Si [83]. These precipitates resist deformation within the grains in the crystal lattice more than the presence of B_4C particles at the grain boundaries. Higher stress is required to overcome the hindrance offered by the Mg_2Si precipitates within the crystal lattice [84]. Because of this higher applied stress compared to the fabricated condition, the deformation step is smaller in the lattice planes due to Mg_2Si precipitates.

The hybrid composites, Al6061–0.1 GNP-1 B_4C responded to the tensile loading by improvement of 97% and 50% in yield and tensile strength in F condition (Fig. 17a and b). The T6 composites also showed an increase of 33% and 20% in yield and tensile strength. These values are 107% and 60% higher than the same composition in the F condition. The contribution of binary reinforcements in the strengthening of the Al6061 matrix can be attributed to a uniform distribution, grain refinement and GNPs anchoring [43]. A maximum decrease in failure strain was recorded for this hybrid SPS composite i.e. 61% and 68% for F and T6, respectively (Fig. 17c). Resistance to deformation arises from the combined effects of GNPs anchoring and dislocation peening due to B_4C particles [17]. The ductility of the Al6061 matrix is greatly compromised by the grain refinement [85]. The additional strength recorded in the tensile tests of hybrid composites can be related to the synergic effect of both reinforcements present in multi-scale distributed uniformly in the Al6061 matrix. The plasticity of the SPSed reference and composites shows a sufficient margin for the employment of secondary processing. It can be deduced that these composites can further be processed in F condition before final shaping and forming into sheets followed by applicable heat treatment for structural applications.

3.6.3. Fractography

All the SPSed reference and composite samples in F and T6 conditions were examined after the tensile tests. Fractography revealed features related to mechanical behaviour and associated strengthening mechanisms. All the SPSed composites with GNPs and B_4C showed improvement in mechanical strength. The Al6061 reference in F and 0.1 wt% GNPs exhibited maximum plasticity (Figs. 16 and 17c). Typical cup and cone fracture [1] propagating within the gauge length cross-section can be seen in Fig. 18a and b for Al6061–F samples. Addition of 0.1 wt% GNPs in the Al6061 matrix partially reduced the ductility. Pulled out GNPs are rarely encountered due to a typical transparent nature of the GNPs at fractional addition (0.1 wt%) in the Al6061 matrix. Comparatively similar ductile failure surfaces (Fig. 18c) were observed for the Al6061–F reference sample. Rarely encountered pulled out GNPs could be seen as shown in Fig. 18d, pointed by the green arrows. These pulled out GNPs represent crack deflection or in simple words resistance to the crack propagation at GNPs junctions/grain boundaries.

Fig. 18e and g shows Al6061-1 B_4C composite in secondary electron mode (SE) and Fig. 18f and h shows backscattered electron mode (BSE). Switching of SEM modes is done to better reveal and identify the B_4C particles. The low magnification Fig. 18e and g shows uniform distribution of 1 wt% B_4C in the Al6061–F matrix. Huge shadowed area in SE mode (Fig. 18e) is evident of bulk area ductile deformation due to comparatively softer matrix and presence of the second phase resulting in overall matrix strengthening. The BSE mode is more sensitive to the density and compared to the depth of field as can be seen in Fig. 18f. Higher magnification (as shown in Fig. 18g) reveals a typical failure of the Al6061 matrix with embedded B_4C particles. These B_4C particles are holding the Al6061 matrix grains by deflecting the crack propagation besides adding bulk dislocation densities in the adjacent Al6061 grains. Fig. 18g and h shows traces of the matrix aluminium (marked with red arrows) strongly adherent to the surface of the B_4C particle. This strong mechanical interface at the surface of B_4C particles offers resistance to the deformation which tends to move the bulk mass. Therefore higher level of stress is required to deform the composite samples containing B_4C particles. This increased strength adversely affects ductility [86].

The hybrid composite containing 0.1 wt% GNPs and 1 wt% B_4C is shown in Fig. 18i-l. B_4C dominated distribution can be seen from the low magnification, Fig. 18i and j. Tracing GNPs in lower 0.1 wt% content is merely difficult however after extensive SEM area scanning, Fig. 18k and l were captured, showing GNPs close to a B_4C particle. As the processing variables for all the SPSed reference and composite samples were kept similar, the tendency of segregation is present due to binary 2nd phase reinforcement in the Al6061 matrix. Fig. 18k shows an area in SE mode with inset taken at a higher resolution to identify the GNPs. Fig. 18l shows the presence of the GNPs in the close vicinity of the B_4C particle. SE and BSE modes revealed the existence of binary reinforcements in the hybrid composite. Severely deformed grains, deep wells associated with the B_4C particles and crack deflation due to the GNPs is prominent. The aforementioned mechanisms resulted in additional strength to the Al6061 matrix. The contrast and elemental distribution associated with the SE and BSE modes explored the revelation of the hybrid reinforcements in the bulk Al6061 matrix.

The fractured surfaces of the T6 set of reference and SPSed composites are shown in Fig. 19. Predominantly, a brittle failure accompanied with a characteristic cleavage can be seen. Fig. 19a shows a low magnification planar fracture surface of the SPSed reference sample in T6. The high magnification of the reference Al6061-T6 sample is shown in Fig. 19b which shows a typical cleavage plane passing through

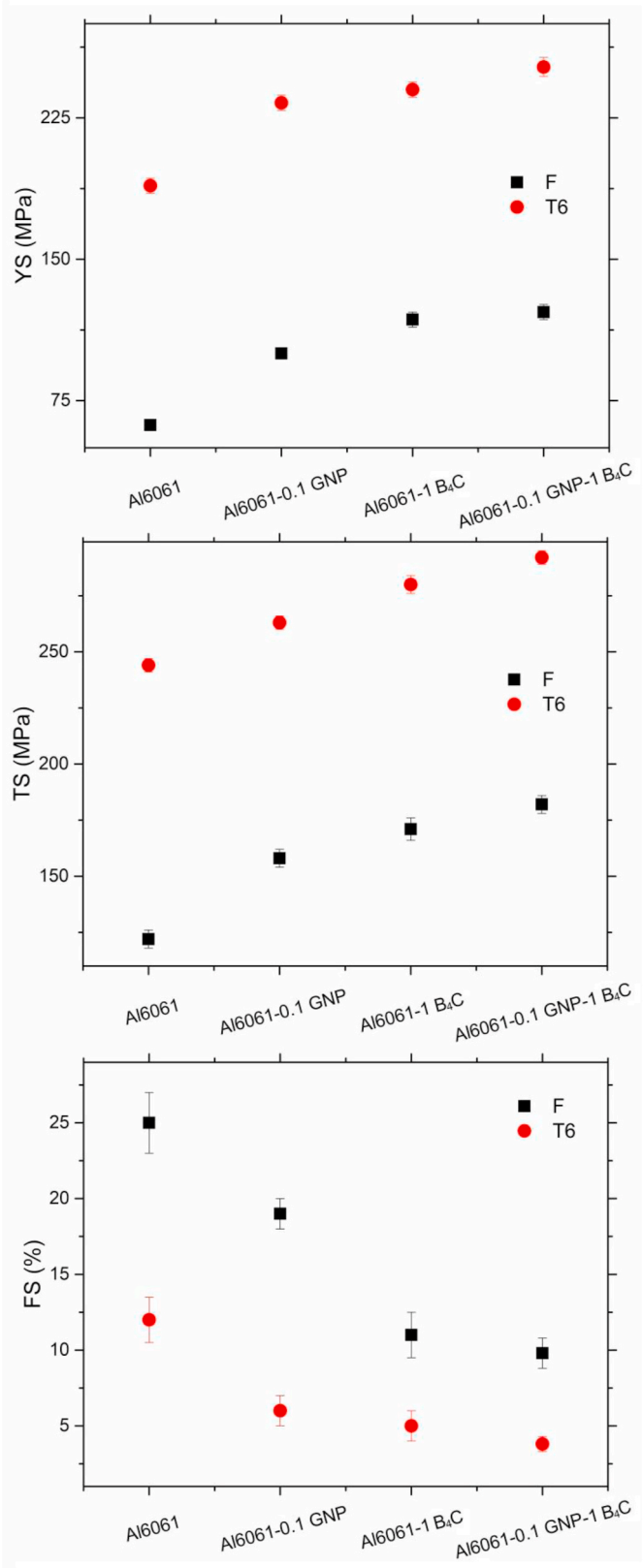

Fig. 17. Tensile testing data plotted with the reinforcement content, showing: a) yield strength, b) tensile strength, and failure strains in F and T6 thermal condition.

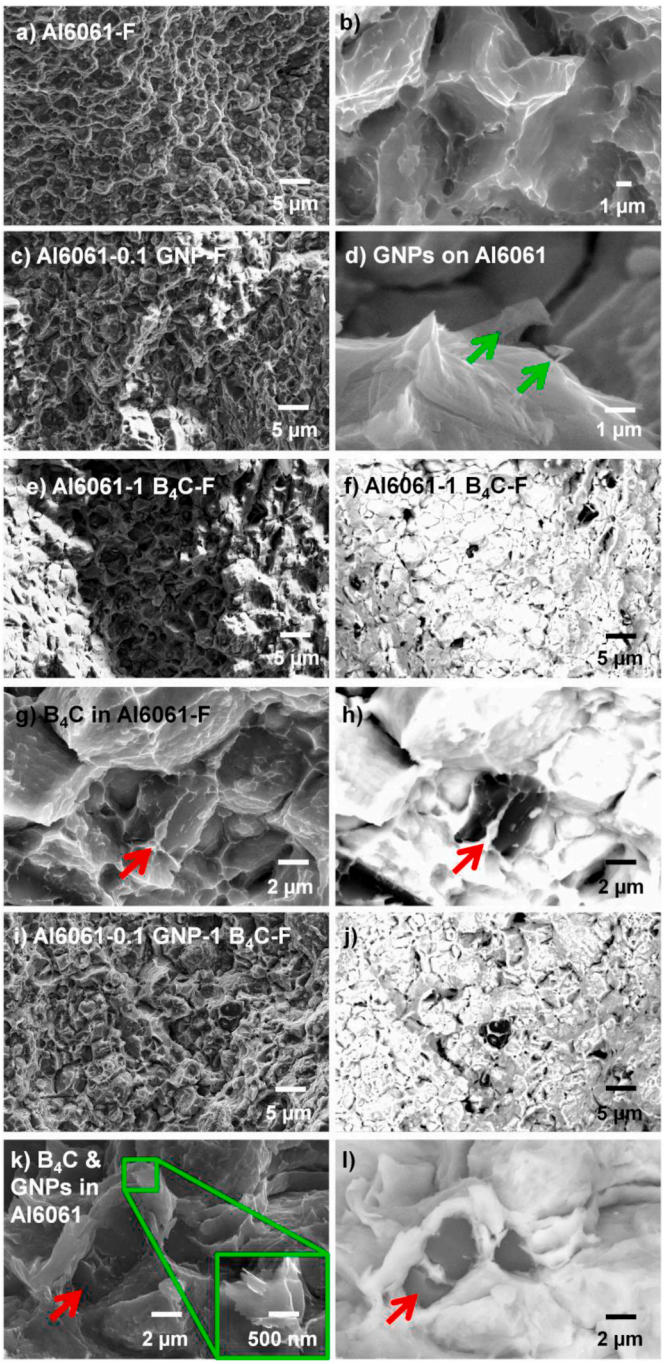

Fig. 18. SEM images of fractured surfaces of a) and b) Al606–F, c) Al6061–0.1 GNP-F, d) GNPs on Al6061, e) Al6061-1 B_4C–F in SE mode, f) Al6061-1 B_4C–F in BSE mode, g) B_4C–F in SE mode, h) B_4C–F in BSE mode, i) Al6061–0.1 GNP-1 B_4C–F in SE mode, j) Al6061–0.1 GNP-1 B_4C–F in BSE mode, k) GNPs and B_4C in Al6061 matrix shown in SE and the same location in l) BSE mode.

smaller deformation steps indicating resistance to the applied stress when compared to Fig. 18b (Al6061–F) which is a characteristic cup & cone, ductile fracture. Fig. 19e and f, show low and high magnification of Al6061-1 B_4C-T6 composite's fractured surface in SE and BSE modes of the same area. A uniform distribution of the B_4C particles can be noticed, complying with the result of optical micrography of the same composite (Figs. 7c and 9e). Fig. 19f shows aluminium adherent on a B_4C particle in the Al6061-1 B_4C-T6 composite, marked with a red arrow. A strong bond of a matrix with reinforcement at the interface is evident from this mechanical interlocking. This strong interfacial

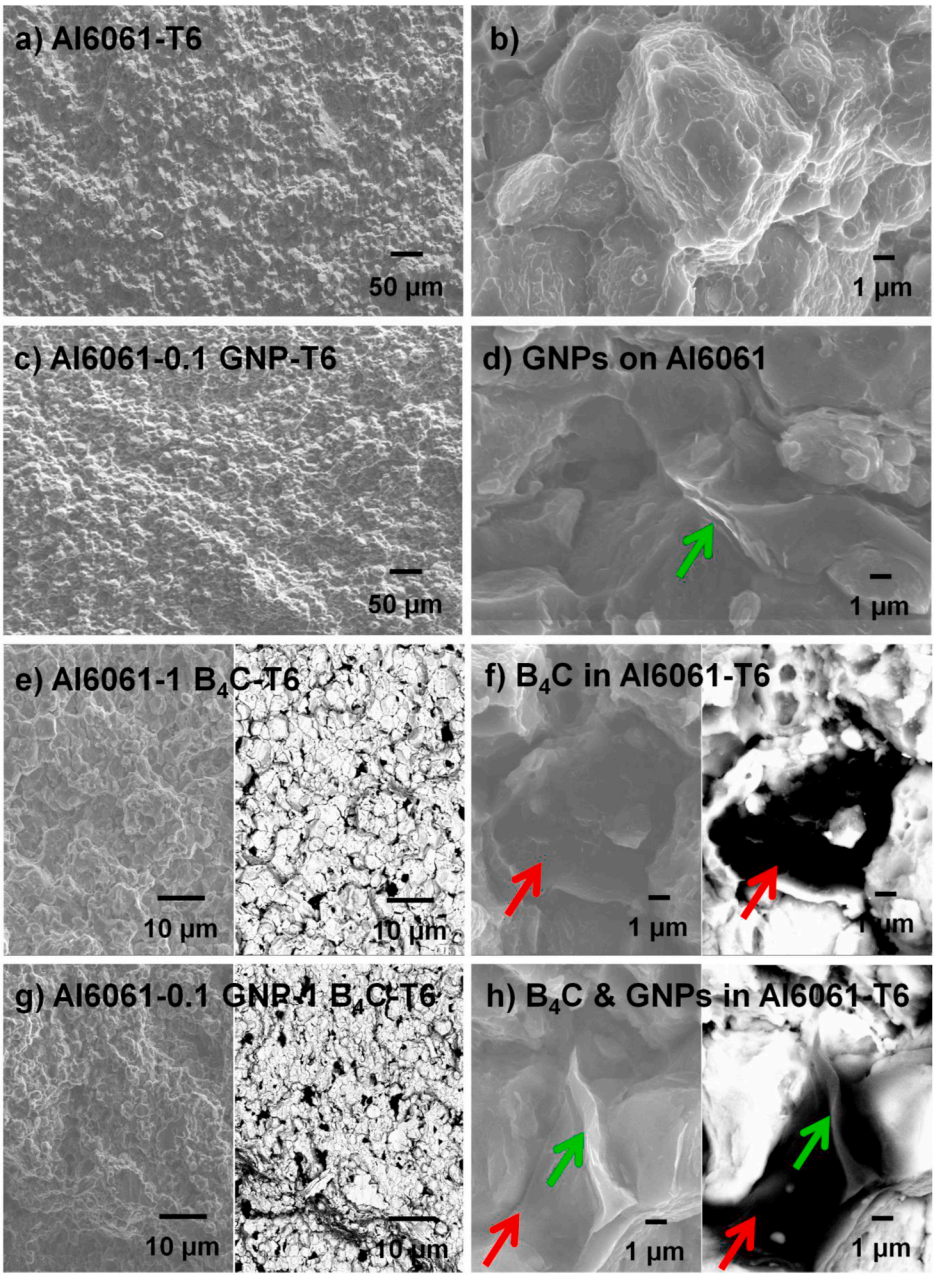

Fig. 19. Fractured surfaces are taken by SEM, for a) & b) Al6061-T6, c) Al6061–0.1 GNP-T6 composite, d) pulled out GNPs in the Al6061-T6 matrix, e) & f) low and high magnifications in SE and BSE modes of Al6061-1 B_4C-T6, respectively, g) & h) low and high magnifications in SE and BSE modes of Al6061–0.1 GNP-1 B_4C-T6, respectively.

bonding of the B_4C/Al6061 leads to an increase in strength compared to the unreinforced Al6061 matrix. XRD results did not show any indication of inter-phase at the reinforcement/matrix interface, thus strengthening the assumption of mechanical interlocking to be factual.

Fig. 19g and h shows hybrid Al6061–0.1 GNP-1 B_4C-T6 composite in high and low magnifications identifying a typical transgranular failure. The low-density gradient due to the difference between the densities of reinforcements and the Al6061 matrix can be expected from the theoretical background of segregation. The densities of GNPs (~2 gm/cm^3), B_4C (~2.5 gm/cm^3) and Al6061 (~2.7 gm/cm^3) are close enough to discourage the segregation. However, due to SPS, as the final processing/sintering step, did not allow sufficient time for the binary reinforcements to segregate. The ball milling operation can be suspected to allow a little bit of segregation. The presence of GNPs is difficult to trace due to their sheet type morphology and optical transparency. Due to extensive SEM exercise, few GNPs were found in the close vicinity of B_4C particles, as shown in Fig. 19h (SE and BSE modes). GNPs are marked with a green arrow and B_4C particles with a red arrow.

Based on the above examination and related discussion, a general illustrative model can be drawn as shown in Fig. 20. Fig. 20a shows GNPs in the Al6061 matrix along with a theoretical crack propagating vertically upwards. As the crack passes through the matrix grains, it encounters GNPs which restrict the movement by hindering the forward propagation until the applied force is sufficient enough to overcome the adhering force of Al6061 with which the GNPs are entrapped and anchored between the matrix grains. Pulled out GNPs, as a result of resisting the propagating crack can be seen in Figs. 18d and 19d. Fig. 20b shows crack deflection in the Al6061 matrix due to a B_4C particle. Due to the different size, aspect ratio and morphology of the B_4C particles from GNPs, the pulled out mechanism is generally specific as crest and trough,

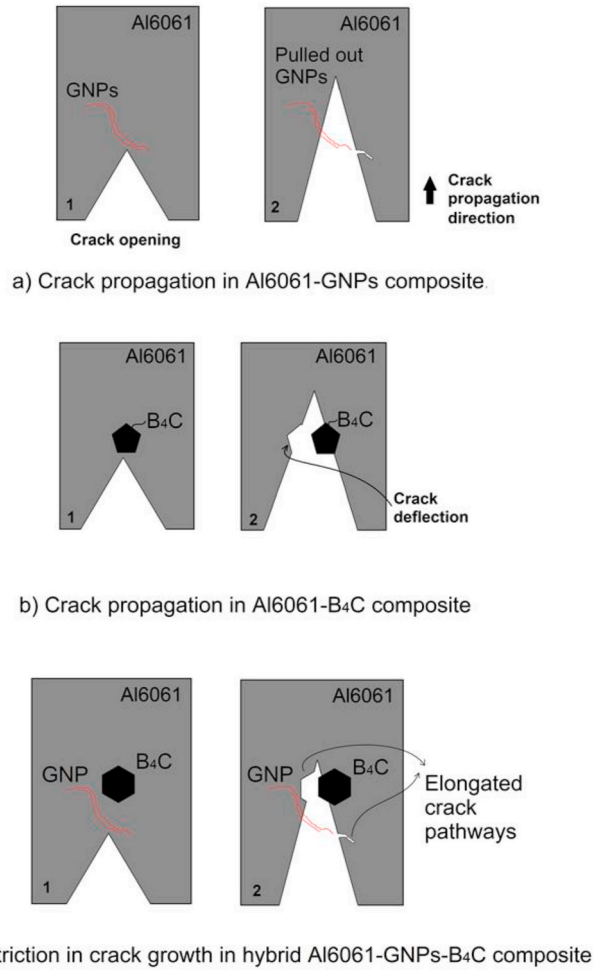

Fig. 20. Illustrative model based on the behaviour of reinforcements in presence of propagating crack in a) Al6061-GNPs composite, b) Al6061–B_4C composites, and c) Al6061-GNPs-B_4C composite.

also known as reinforcement wells for B_4C particles. Combined effects of GNPs and B_4C particle greatly restricts the resistance to deformation and crack propagation along with the deflection thus resulting in enhanced Al6061 matrix strength. Fig. 20c shows the presence of GNPs and B_4C on the principal axis of crack propagation. Owing to the uniform distribution of GNPs and B_4C, the probability of micro-cracks encountering dual reinforcement at the principal axis is expected to be the maximum. The increased mechanical properties affirm this presumption as illustrated by the model in Fig. 20. The models presented in the present study help better understanding of physical phenomenon behind the strengthening mechanism of such a novel class of composites processed via SPS.

4. Conclusions

The GNPs and B_4C demonstrated improved mechanical properties in the Al6061 matrix. Their contribution in the strengthening of the Al6061 matrix, as an individual and in hybrid combination was evaluated with a detailed investigation on microstructure evolution using EBSD, assisted by OM and SEM. Effects of SPS processing and the resulting microstructures are correlated with the mechanical performance of the composites and other relevant studies. The results encouraged the potential use of Al-GNPs, Al–B_4C and Al-GNPs-B_4C composites for the futuristic design of low weight and high strength applications of the automobile and aerospace industry. Following conclusions can be drawn from the proceeding discussion:

1. The evolved microstructure at the selected ball milling parameters revealed uniform distribution of the reinforcements in the Al6061 matrix. No lumps or agglomerates of GNPs and/or B_4C particles were observed in OM and SEM.
2. Ductility of the Al6061 matrix entrapped GNPs by mechanical alloying. Nearly theoretical densities of the SPSed reference and composite samples were achieved, owing to the better compaction and sintering during SPS.
3. SEM and FTIR results showed the effectiveness of employing a dual dispersion technique for exfoliation of GNPs, namely: solution sonication and ball milling. Raman spectroscopy confirmed the signatures of GNPs and endorsed the efficacy of the dual dispersion technique.
4. XRD analysis showed typical characteristic peaks of Aluminium with no detectable peaks of any other phase or intermetallics.
5. EBSD analysis revealed the effects of GNPs and B_4C on the microstructure. The incremental trend in grain boundary mismatch is recorded corresponding to the increasing distribution of GNPs in the Al6061 matrix compared to the B_4C reinforced composites.
6. The interphase free and clean interface was observed in SEM examination of GNPs and B_4C composites owning to short sintering time and solid-state SPS processing. A strong mechanical bond with entrapped and mechanically alloyed GNPs in the Al6061 matrix was achieved. Similarly, B_4C and Al6061 matrix maintained an adherent mechanically bond with no intermetallic phase between them.
7. The hardness of the Al6061 matrix was found to increase with the addition of GNPs and B_4C. 18%, 27% and 33% increase in hardness was found in F condition and 11%, 22% and 25% in the T6 condition. The contribution of GNPs and B_4C to result in increased hardness is higher in the F condition compared to the T6 thermal condition.
8. Tensile test results followed the hardness test trend and revealed excellent ductility of the SPSed reference and composites. Hybrid composite of GNPs and B_4C yielded maximum tensile strength (YS 33% and TS 20%) in the T6 condition. Dislocation peening at the reinforcement interface and grain boundaries anchoring was found to be the responsible mechanisms for the additional strength exhibited by the SPSed composites of GNPs and B_4C.
9. Severely deformed grains as seen in fractured surfaces with uniformly distributed and pulled out GNPs and/or embedded B_4C in Al6061 matrix reveal near theoretical densities owing to better compaction and sintering. Fractography revealed the presence of GNPs and B_4C at the nodal points of the grains with pulled out appearance. Thus strengthening the grain anchoring and crack deflection postulates which are related to the strengthening mechanisms.

CRediT authorship contribution statement

Mahmood Khan: Conceptualization, Methodology, Investigation, Validation, Writing – original draft. **Rafi Ud Din:** Methodology, Investigation, Formal analysis. **Muhammad Abdul Basit:** Writing – review & editing. **Abdul Wadood:** Writing – original draft, Writing – review & editing. **Syed Wilayat Husain:** Conceptualization, Project administration, Supervision. **Shahid Akhtar:** Writing – review & editing, Resources. **Ragnhild Elizabeth Aune:** Methodology, Resources, Funding acquisition.

Declaration of competing interest

The authors declare that they have no known competing financial interests or personal relationships that could have appeared to influence the work reported in this paper.

Acknowledgements

The authors acknowledge the financial support of the Higher

Education Commission of Pakistan (Grant No. 213-53249-2EG2-102) provided under the PhD indigenous fellowship; Phase-II Batch-II, as well as the Norwegian University of Science and Technology (NTNU), Norway, for the use of their laboratory facilities for processing and characterization.

References

[1] M. Khan, M. Amjad, A. Khan, R. Ud-Din, I. Ahmad, T. Subhani, Microstructural evolution, mechanical profile, and fracture morphology of aluminum matrix composites containing graphene nanoplatelets, Journal of Materials Research (2017) 1–12.

[2] M. Khan, M. Zulfaqar, F. Ali, T. Subhani, Hybrid aluminium matrix composites containing boron carbide and quasicrystals: manufacturing and characterisation, Materials Science and Technology 33 (16) (2017) 1955–1963, 2017/11/02.

[3] H.A. Alhashmy, M. Nganbe, Laminate squeeze casting of carbon fiber reinforced aluminum matrix composites, Materials & Design 67 (2015) 154–158, 2/15/.

[4] M. Khan, A. Rehman, T. Aziz, K. Naveed, I. Ahmad, T. Subhani, Cold formability of friction stir processed aluminum composites containing carbon nanotubes and boron carbide particles, Materials Science and Engineering: A 696 (2017) 552–557, 2017/06/01/.

[5] S.R. Vladislav Domnich, Richard A. Haber, Manish Chhowalla, Boron carbide: structure, properties, and stability under stress, Journal of the American Ceramic Society 94 (11) (2011) 24.

[6] M. Khan, M. Zulfaqar, F. Ali, T. Subhani, Microstructural and mechanical characterization of hybrid aluminum matrix composite containing boron carbide and Al-Cu-Fe quasicrystals, Metals and Materials International 23 (4) (July 01, 2017) 813–822.

[7] M. Khan, A. Rehman, T. Aziz, M. Shahzad, K. Naveed, T. Subhani, Effect of inter-cavity spacing in friction stir processed Al 5083 composites containing carbon nanotubes and boron carbide particles, Journal of Materials Processing Technology 253 (2018) 72–85, 2018/03/01/.

[8] B. Chen, S. Li, H. Imai, J. Umeda, M. Takahashi, K. Kondoh, Inter-wall bridging induced peeling of multi-walled carbon nanotubes during tensile failure in aluminum matrix composites, Micron 69 (2015) 1–5, 2//.

[9] L.A. Yolshina, R.V. Muradymov, I.V. Korsun, G.A. Yakovlev, S.V. Smirnov, Novel aluminum-graphene and aluminum-graphite metallic composite materials: synthesis and properties, Journal of Alloys and Compounds 663 (2016) 449–459, 2016/04/05/.

[10] Z. Xu, in: Graphene H. Zhu, Z. Xu, D. Xie, Y. Fang (Eds.), Fundamental Properties of Graphene, Academic Press, United States, 2018, pp. 73–102.

[11] X. Huang, X. Qi, F. Boey, H. Zhang, Graphene-based composites, Chemical Society Reviews 41 (2) (2012) 666–686.

[12] W. Yang, Q. Zhao, L. Xin, J. Qiao, J. Zou, P. Shao, Z. Yu, Q. Zhang, G. Wu, Microstructure and mechanical properties of graphene nanoplates reinforced pure Al matrix composites prepared by pressure infiltration method, Journal of Alloys and Compounds 732 (Supplement C) (2018) 748–758, 2018/01/25/.

[13] B. Ravi, B.B. Naik, J.U. Prakash, Characterization of aluminium matrix composites (AA6061/B4C) fabricated by stir casting technique, Materials Today: Proceedings 2 (4–5) (2015) 2984–2990.

[14] X.-f. Tan, F.-h. Zeng, S.-q. Wang, F. Zhou, X. Xiong, Effects of heat treatment on phase contents and mechanical properties of infiltrated B4C/2024Al composites, Transactions of Nonferrous Metals Society of China 24 (7) (2014) 2359–2365, 7//.

[15] M. Ipekoglu, A. Nekouyan, O. Albayrak, S. Altintas, Mechanical characterization of B4C reinforced aluminum matrix composites produced by squeeze casting, Journal of Materials Research 32 (3) (2017) 599–605.

[16] M. Khan, W. H. Syed, S. Akhtar, and R. E. Aune, "Friction stir processing (FSP) of multiwall carbon nanotubes and boron carbide reinforced aluminum alloy (Al 5083) composites," Friction Stir Welding and Processing X. pp. 217-232.

[17] M. Khan, R. Ud-Din, W. H. Syed, S. Akhtar, and R. E. Aune, "Spark plasma sintering of boron carbide reinforced aluminum alloy (Al6061) matrix composites," Proceedings of 2019 16th International Bhurban Conference on Applied Sciences & Technology (IBCAST). pp. 35-41.

[18] J. Liu, U. Khan, J. Coleman, B. Fernandez, P. Rodriguez, S. Naher, D. Brabazon, Graphene oxide and graphene nanosheet reinforced aluminium matrix composites: powder synthesis and prepared composite characteristics, Materials & Design 94 (2016) 87–94, 3/15/.

[19] Y.T. Zhou, Y.N. Zan, S.J. Zheng, Q.Z. Wang, B.L. Xiao, X.L. Ma, Z.Y. Ma, Distribution of the microalloying element Cu in B4C-reinforced 6061Al composites, Journal of Alloys and Compounds 728 (2017) 112–117, 2017/12/25/.

[20] H. Zhang, K.T. Ramesh, E.S.C. Chin, High strain rate response of aluminum 6092/B4C composites, Materials Science and Engineering: A 384 (1–2) (2004) 26–34, 10/25/.

[21] A. Abdollahi, A. Alizadeh, H.R. Baharvandi, "Dry sliding tribological behavior and mechanical properties of Al2024–5 wt.%B4C nanocomposite produced by mechanical milling and hot extrusion, Materials & Design 55 (2014) 471–481, 3//.

[22] M. Naseri, A. Hassani, M. Tajally, An alternative method for manufacturing Al/B4C/SiC hybrid composite strips by cross accumulative roll bonding (CARB) process, Part A, Ceramics International 41 (10) (2015) 13461–13469, 12//.

[23] H.S. Chen, W.X. Wang, Y.L. Li, P. Zhang, H.H. Nie, Q.C. Wu, The design, microstructure and tensile properties of B4C particulate reinforced 6061Al neutron absorber composites, 2015/05/25/, Journal of Alloys and Compounds 632 (2015) 23–29.

[24] C.S. Ramesh, R. Keshavamurthy, J. Madhusudhan, Fatigue behavior of Ni-P coated Si3N4 reinforced Al6061 composites, Procedia Materials Science 6 (2014) 1444–1454.

[25] C. Cheng, Y. Wu, Y. Qu, R. Ma, R. Fan, Radio-frequency negative permittivity of carbon nanotube/copper calcium titanate ceramic nanocomposites fabricated by spark plasma sintering, 2020/02/01/, Ceramics International 46 (2) (2020) 2261–2267.

[26] Z.A. Munir, U. Anselmi-Tamburini, M. Ohyanagi, The effect of electric field and pressure on the synthesis and consolidation of materials: a review of the spark plasma sintering method, Journal of Materials Science 41 (3) (February 01, 2006) 763–777.

[27] Y. Lian, Z. Yang, J. Yang, C. Mao, Processing and mechanical properties of 2024 aluminum matrix composites containing Tungsten and Tantalum prepared by PM, 12//, Rare Metals 25 (6, Supplement 2) (2006) 136–140.

[28] Z.-F. Liu, Z.-H. Zhang, J.-F. Lu, A.V. Korznikov, E. Korznikova, F.-C. Wang, Effect of sintering temperature on microstructures and mechanical properties of spark plasma sintered nanocrystalline aluminum, 2014/12/01/, Materials & Design 64 (2014) 625–630.

[29] Y. Wu, K. Zhan, Z. Yang, W. Sun, B. Zhao, Y. Yan, J. Yang, Graphene oxide/Al composites with enhanced mechanical properties fabricated by simple electrostatic interaction and powder metallurgy, 2019/02/15/, Journal of Alloys and Compounds 775 (2019) 233–240.

[30] S.J. Yan, S.L. Dai, X.Y. Zhang, C. Yang, Q.H. Hong, J.Z. Chen, Z.M. Lin, Investigating aluminum alloy reinforced by graphene nanoflakes, 2014/08/26/, Materials Science and Engineering: A 612 (Supplement C) (2014) 440–444.

[31] A. Ghazaly, B. Seif, H.G. Salem, Mechanical and tribological properties of AA2124-graphene self lubricating nanocomposite, Light Metals (2013) 411–415. John Wiley & Sons, Inc., 2013.

[32] M. Fattahi, A.R. Gholami, A. Eynalvandpour, E. Ahmadi, Y. Fattahi, S. Akhavan, Improved microstructure and mechanical properties in gas tungsten arc welded aluminum joints by using graphene nanosheets/aluminum composite filler wires, 9//, Micron 64 (2014) 20–27.

[33] Q. Abbas shafqat, u. Rafi-ud-din, M. Shahzad, M. Khan, S. Mehmood, W.A. Syed, A. Basit, N. Mehboob, T. Ali, Mechanical, tribological, and electrochemical behavior of hybrid aluminum matrix composite containing boron carbide (B4C) and graphene nanoplatelets, Journal of Materials Research 34 (18) (2019) 3116–3129.

[34] V. Umasankar, M. Anthony Xavior, S. Karthikeyan, Experimental evaluation of the influence of processing parameters on the mechanical properties of SiC particle reinforced AA6061 aluminium alloy matrix composite by powder processing, Journal of Alloys and Compounds 582 (2014) 380–386, 1/5/.

[35] A.J. Knowles, X. Jiang, M. Galano, F. Audebert, Microstructure and mechanical properties of 6061 Al alloy based composites with SiC nanoparticles, Journal of Alloys and Compounds 615 (Supplement 1) (2014) S401–S405, 12/5/.

[36] J. Rams, A. Ureña, M.D. Escalera, M. Sánchez, Electroless nickel coated short carbon fibres in aluminium matrix composites, Composites Part A: Applied Science and Manufacturing 38 (2) (2007) 566–575, 2//.

[37] H. Kwon, D.H. Park, J.F. Silvain, A. Kawasaki, Investigation of carbon nanotube reinforced aluminum matrix composite materials, Composites Science and Technology 70 (3) (2010) 546–550, 2010/03/01/.

[38] M. Bastwros, G.-Y. Kim, C. Zhu, K. Zhang, S. Wang, X. Tang, X. Wang, Effect of ball milling on graphene reinforced Al6061 composite fabricated by semi-solid sintering, Composites Part B: Engineering 60 (Supplement C) (2014) 111–118, 2014/04/01/.

[39] M.C. Şenel, M. Gürbüz, E. Koç, "Fabrication and Characterization of Synergistic Al-SiC-GNPs Hybrid Composites," *Composites Part B: Engineering*, 2018, 2018/07/20/.

[40] A. Saghar, M. Khan, I. Sadiq, T. Subhani, Effect of carbon nanotubes and silicon carbide particles on ablative properties of carbon fiber phenolic matrix composites, Vacuum 148 (2018) 124–126, 2018/02/01/.

[41] W.-W. Liu, B.-Y. Xia, X.-X. Wang, J.-N. Wang, Exfoliation and dispersion of graphene in ethanol-water mixtures, Frontiers of Materials Science 6 (2) (2012) 176–182, 2012/06/01.

[42] J.-M. Ju, G. Wang, K.-H. Sim, Facile synthesis of graphene reinforced Al matrix composites with improved dispersion of graphene and enhanced mechanical properties, Journal of Alloys and Compounds 704 (Supplement C) (2017) 585–592, 2017/05/15/.

[43] M. Khan, R. Ud Din, A. Wadood, W.H. Syed, S. Akhtar, R.E. Aune, Effect of graphene nanoplatelets on the physical and mechanical properties of Al6061 in fabricated and T6 thermal conditions, Journal of Alloys and Compounds 790 (2019) 1076–1091, 2019/06/25/.

[44] R.U. Din, Q.A. Shafqat, Z. Asghar, G.H. Zahid, A. Basit, A.H. Qureshi, T. Manzoor, M.A. Nasir, F. Mehmood, K.I. Hussain, "Microstructural evolution, powder characteristics, compaction behavior and sinterability of Al 6061–B4C composites as a function of reinforcement content and milling times, Russian Journal of Non-Ferrous Metals 59 (2) (March 01, 2018) 207–222.

[45] F. Fondeur, J.L. Koenig, FT-IR characterization of the surface of aluminum as a result of chemical treatment, The Journal of Adhesion 40 (2–4) (1993) 189–205, 1993/05/01.

[46] X. Li, J. Wu, C. Tang, Z. He, P. Yuan, Y. Sun, W.-m. Lau, K. Zhang, J. Mei, Y. Huang, High temperature resistant polyimide/boron carbide composites for neutron radiation shielding, Composites Part B: Engineering 159 (2019) 355–361, 2019/02/15/.

[47] M. Remanan, R.S. Rao, S. Bhowmik, L. Varshney, M. Abraham, K. Jayanarayanan, Hybrid nanocomposites based on poly aryl ether ketone, boron carbide and multi walled carbon nanotubes: evaluation of tensile, dynamic mechanical and thermal degradation properties, e-Polymers 16 (6) (2016) 493–503.

[48] M.W. Mortensen, P.G. Sørensen, O. Björkdahl, M.R. Jensen, H.J.G. Gundersen, T. Bjørnholm, Preparation and characterization of Boron carbide nanoparticles for use as a novel agent in T cell-guided boron neutron capture therapy, Applied Radiation and Isotopes 64 (3) (2006) 315–324, 2006/03/01/.
[49] A. Hadi, J. Zahirifar, J. Karimi-Sabet, A. Dastbaz, Graphene Nanosheets Preparation Using Magnetic Nanoparticle Assisted Liquid Phase Exfoliation of Graphite: the Coupled Effect of Ultrasound and Wedging Nanoparticles, 2018.
[50] Z. Çiplak, N. Yildiz, A. Çalimli, Investigation of graphene/Ag nanocomposites synthesis parameters for two different synthesis methods," *fullerenes*, Nanotubes and Carbon Nanostructures 23 (4) (2015) 361–370, 2015/04/03.
[51] D. He, Z. Peng, W. Gong, Y. Luo, P. Zhao, L. Kong, Mechanism of a green graphene oxide reduction with reusable potassium carbonate, RSC Advances 5 (16) (2015) 11966–11972.
[52] S. Jaworski, M. Wierzbicki, E. Sawosz, A. Jung, G. Gielerak, J. Biernat, H. Jaremek, W. Łojkowski, B. Woźniak, J. Wojnarowicz, L. Stobiński, A. Małolepszy, M. Mazurkiewicz-Pawlicka, M. Łojkowski, N. Kurantowicz, A. Chwalibog, Graphene oxide-based nanocomposites decorated with silver nanoparticles as an antibacterial agent, Nanoscale Research Letters 13 (1) (2018) 116. April 23.
[53] V. Ţucureanu, A. Matei, A.M. Avram, FTIR spectroscopy for carbon family study, Critical Reviews in Analytical Chemistry 46 (6) (2016) 502–520, 2016/11/01.
[54] Y. Gao, W. Shi, W. Wang, Y. Wang, Y. Zhao, Z. Lei, R. Miao, Ultrasonic-assisted production of graphene with high yield in supercritical CO2 and its high electrical conductivity film, Industrial & Engineering Chemistry Research 53 (7) (2014) 2839–2845, 2014/02/19.
[55] M.A. Saiful Badri, M. Mat Salleh, N.F. Md Noor, M. Y. Abd Rahman, A. Ali Umar, Green Synthesis of Few-Layered Graphene from Aqueous Processed Graphite Exfoliation for Graphene Thin Film Preparation, 2017.
[56] K.M. Reddy, P. Liu, A. Hirata, T. Fujita, M.W. Chen, Atomic structure of amorphous shear bands in boron carbide, Nature Communications 4 (2013) 2483, 09/19/ online.
[57] X.-C. Wei, Y.-L. Xu, N. Meng, Y. Xu, A. Hakro, G.-L. Dai, R. Hao, E.-P. Li, A non-contact graphene surface scattering rate characterization method at microwave frequency by combining Raman spectroscopy and coaxial connectors measurement, 10//, Carbon 77 (2014) 53–58.
[58] C. Damm, T.J. Nacken, W. Peukert, Quantitative evaluation of delamination of graphite by wet media milling, Carbon 81 (2015) 284–294, 2015/01/01/.
[59] X. Cai, Z. Jiang, X. Zhang, X. Zhang, Effects of tip sonication parameters on liquid phase exfoliation of graphite into graphene nanoplatelets, August 17, Nanoscale Research Letters 13 (1) (2018) 241.
[60] R. Maurya, B. Kumar, S. Ariharan, J. Ramkumar, K. Balani, Effect of carbonaceous reinforcements on the mechanical and tribological properties of friction stir processed Al6061 alloy, 5/15/, Materials & Design 98 (2016) 155–166.
[61] Z.W. Zhang, Z.Y. Liu, B.L. Xiao, D.R. Ni, Z.Y. Ma, High efficiency dispersal and strengthening of graphene reinforced aluminum alloy composites fabricated by powder metallurgy combined with friction stir processing, 2018/08/01/, Carbon 135 (2018) 215–223.
[62] G. Victor, Y. Pipon, N. Bérerd, N. Toulhoat, N. Moncoffre, N. Djourelov, S. Miro, J. Baillet, N. Pradeilles, O. Rapaud, A. Maître, D. Gosset, Structural modifications induced by ion irradiation and temperature in boron carbide B4C, Nuclear Instruments and Methods in Physics Research Section B: Beam Interactions with Materials and Atoms 365 (2015) 30–34, 2015/12/15/.
[63] M. Naranjo, X. Rodrı, J.A. Guez, E.J. Herrera, "Sintering of Al/AlN composite powder obtained by gas–solid reaction milling, Scripta Materialia 49 (1) (2003) 65–69, 7//.
[64] N. Chawla, K.K. Chawla, Metal Matrix Composites, Springer, New York, 2013.
[65] M. Ipekoglu, A. Nekouyan, O. Albayrak, S. Altintas, Mechanical characterization of B 4 C reinforced aluminum matrix composites produced by squeeze casting, Journal of Materials Research (2017) 1–7.
[66] J. Campbell, Complete Casting Handbook: Metal Casting Processes, Metallurgy, Techniques and Design, Elsevier Butterworth-Heinemann, 2011.
[67] M. Antadze, R. Chedia, O. Tsagareishvili, A. Mikeladze, A. Gacheciladze, B. Margiev, D. Gabunia, T. Tsuladze, D. Khantadze, Metal-ceramics based on nanostructured boron carbide, 11//, Solid State Sciences 14 (11–12) (2012) 1725–1728.
[68] L. Chen, Y. Qi, Y. Fei, Z. Du, Enhanced mechanical properties and thermal conductivity for GNPs/Al2024 composites with in situ SiC nanorods, Metals and Materials International 14 (2020) 1–8, https://doi.org/10.1007/s12540-020-00803-9.
[69] A. Saboori, M. Pavese, C. Badini, P. Fino, "Microstructure and thermal conductivity of Al–graphene composites fabricated by powder metallurgy and hot rolling techniques, Acta Metallurgica Sinica (English Letters) 30 (7) (July 01, 2017) 675–687.
[70] H.-s. Chen, W.-x. Wang, H.-h. Nie, J. Zhou, Y.-l. Li, P. Zhang, Microstructure and mechanical properties of B4C/6061Al laminar composites fabricated by power metallurgy, Vacuum 143 (2017) 363–370, 2017/09/01/.
[71] G. Liu, N. Zhao, C. Shi, E. Liu, F. He, L. Ma, Q. Li, J. Li, C. He, In-situ synthesis of graphene decorated with nickel nanoparticles for fabricating reinforced 6061Al matrix composites, 2017/06/24/, Materials Science and Engineering: A 699 (Supplement C) (2017) 185–193.
[72] W.-m. Tian, S.-m. Li, B. Wang, X. Chen, J.-h. Liu, M. Yu, Graphene-reinforced aluminum matrix composites prepared by spark plasma sintering, International Journal of Minerals, Metallurgy, and Materials 23 (6) (2016) 723–729.
[73] M. Khan, R. Ud-Din, A. Wadood, S.W. Husain, S. Akhtar, R.E. Aune, Physical and mechanical properties of graphene nanoplatelet-reinforced Al6061-T6 composites processed by spark plasma sintering, 2020/03/31, JOM 72 (6) (2020) 2295–2304, https://doi.org/10.1007/s11837-020-04139-y.
[74] H. Zhang, C. Xu, W. Xiao, K. Ameyama, C. Ma, Enhanced mechanical properties of Al5083 alloy with graphene nanoplates prepared by ball milling and hot extrusion, 2016/03/21/, Materials Science and Engineering: A 658 (2016) 8–15.
[75] Z. Asghar, M.A. Latif, D. Rafi ud, Z. Nazar, F. Ali, A. Basit, S. Badshah, T. Subhani, Effect of distribution of B4C on the mechanical behaviour of Al-6061/B4C composite, 2018/08/08, Powder Metallurgy 61 (4) (2018) 293–300.
[76] A.J. Schwartz, M. Kumar, B.L. Adams, D.P. Field, Electron Backscatter Diffraction in Materials Science, Springer, 2000.
[77] C. Maurice, R. Fortunier, A 3D Hough transform for indexing EBSD and Kossel patterns, Journal of Microscopy 230 (3) (2008) 520–529.
[78] Z. Du, M.J. Tan, J.F. Guo, G. Bi, J. Wei, Fabrication of a new Al-Al2O3-CNTs composite using friction stir processing (FSP), 6/14/, Materials Science and Engineering: A 667 (2016) 125–131.
[79] Z. Asghar, G.H. Zahid, D. Rafi ud, E. Ahmad, M. Mehmood, S. Badshah, Effect of degassing parameters on sinterability of Al/B4C powder mixture, 2015/03/31, Powder Metallurgy 58 (1) (2015) 36–40.
[80] F.H. Latief, E.-S.M. Sherif, A.A. Almajid, H. Junaedi, Fabrication of exfoliated graphite nanoplatelets-reinforced aluminum composites and evaluating their mechanical properties and corrosion behavior, Journal of Analytical and Applied Pyrolysis 92 (2) (2011) 485–492, 11//.
[81] M.M. El-Rayes, E.A. El-Danaf, The influence of multi-pass friction stir processing on the microstructural and mechanical properties of Aluminum Alloy 6082, Journal of Materials Processing Technology 212 (5) (2012) 1157–1168, 5//.
[82] V. Sharma, U. Prakash, B.V.M. Kumar, Surface composites by friction stir processing: a review, Journal of Materials Processing Technology 224 (2015) 117–134, 10//.
[83] Y. Lee, Y. Kwon, J. Lee, C. Park, S. Kim, Effects of strain and strain rate on tensile behavior of hot-forged Al 6061-T6, Materials Science and Engineering: A 362 (1) (2003) 187–191, 2003/12/05/.
[84] M.E. Kassner, P. Geantil, X. Li, A study of the quench sensitivity of 6061-T6 and 6069-T6 aluminum alloys, Journal of Metallurgy (2011) 2011.
[85] Y.Z. Li, Q.Z. Wang, W.G. Wang, B.L. Xiao, Z.Y. Ma, Effect of interfacial reaction on age-hardening ability of B4C/6061Al composites, Materials Science and Engineering: A 620 (2015) 445–453, 2015/01/03/.
[86] H. Yang, T.D. Topping, K. Wehage, L. Jiang, E.J. Lavernia, J.M. Schoenung, Tensile behavior and strengthening mechanisms in a submicron B4C-reinforced Al trimodal composite, Materials Science and Engineering: A 616 (2014) 35–43, 10/20/.